A SEARCH FOR $2\nu\beta\beta$-DECAY OF ^{130}Te TO THE FIRST EXCITED 0^+ STATE IN ^{130}Xe WITH THE CUORICINO DETECTOR

by

Iulian Catalin Bandac

Bachelor of Science
Alexandru Ioan Cuza University of Iasi, Romania, 1994

Master of Science
Alexandru Ioan Cuza University of Iasi, Romania 1996

Submitted in Partial Fulfillment of the Requirements

for the Degree of Doctor of Philosophy in the

Department of Physics and Astronomy

College of Arts and Sciences

University of South Carolina

2006

Major Professor	Committee Member
Committee Member	Chairman, Examining Committee
Committee Member	Dean of The Graduate School

To my Kati . . .

Acknowledgments

I have been lucky to have Prof. Frank Avignone as my thesis supervisor. Without his academic insights and ever-encouraging comments, I am certain that I would be still far away from the finish line. Thanks to my readers Prof. Oliviero Cremonesi, Prof. Richard Creswick, Prof. Christina Lacey and Prof. John Palms. They patiently went through my thesis and pointed out errors and unclear explanations.

I would like to thank Carlo Bucci, Stefano Pirro, Paolo Gorla, Maura Pavan, Silvia Capelli and Lidia Torres for very constructive discussions.

I wish to say thanks to my parents, to my daughter Alexandra and to my fiancée Kati for their unconditional love, support and encouragement.

I also wish to thank Alex Asandei, Ricardo Artusa, Rodney Topp and Gheorghe Zet for their support and friendship.

ABSTRACT

A SEARCH FOR $2\nu\beta\beta$-DECAY OF ^{130}Te TO THE FIRST EXCITED 0^+ STATE IN ^{130}Xe WITH THE CUORICINO DETECTOR

Iulian Catalin Bandac

An overview of the subject of zero neutrino double beta decay is given beginning with the general properties of neutrinos. These include neutrino mixing, neutrino mixing matrix, and the parameters obtained from neutrino oscillation experiments. A brief history of the subject of double-beta $(\beta\beta)$ decay is given, followed by discussion of the salient points of the underlying theoretical formalism and its connection to the theory of neutrinos, and in particular its direct connection of neutrino mixing matrix. A brief discussion is given of the foundations of the Quasi Particle Random Phase Approximation (QRPA) method of calculating the relevant nuclear transition matrix elements. This is followed by a detailed description of the Bolometric Technique of detecting particles and radiation, and its direct application to $\beta\beta$-decay. The structure and construction of the CUORICINO bolometric detector is discussed in detail, as well as its operation to collect the data used in the research that is the subject of this dissertation. The detector comprises 13 planes of TeO_2 bolometers containing 40.7 kg of crystals, with a total of 11 kg of ^{130}Te. Finally, a detailed discussion of data acquisition and analysis, and a presentation of the final results is given. The main goal of the experimental effort of the author was to search for $\beta\beta$-decay of ^{130}Te to the first excited 0^+ state at 1793.50 keV in ^{130}Xe. The detector was operated for a total exposure of $Nt = 2.764 \times 10^{25}$ y. The detection efficiency was computed with a Monte Carlo simulation of the complete detector. The result is $\varepsilon = 0.011$. The final result for the decay to the excited state is: $T^{2\nu}_{1/2} = \left(1.45^{+1.23}_{-0.46}\right) \times 10^{22}$ y. While this a positive result, it is not statistically significant. In any case a lower limit can be stated: $T^{2\nu}_{1/2} \geq 0.90 \times 10^{22}$ y (90% C.L.). If the small positive peak in the data is due to $\beta\beta$-decay, two more years of running should give a conclusive observation. The data were analyzed to search for $0\nu\beta\beta$-decay of

^{130}Te to the ^{130}Xe ground state with the resulting lower bound of $T^{0\nu}_{1/2}(^{130}Te) \geq 1.84\times10^{24}$ y using the most conservative interpretation of the data.

Dissertation Director: Dr. Frank T. Avignone III

Contents

List of Tables

List of Figures

Preface

In general, nature is extremely close to what the Weinberg-Salam theory predicts. The fact that neutrino physics is of great interest today arises from the hope that the physics of neutrino might lead to new physics, beyond the standard theory.[31]

Until now it is believed that the neutrino is the only particle which is free from interactions stronger than the weak interaction. We may hope that a weaker interaction would be most apparent in the physics of neutrinos. Another important aspect is that the mass of the neutrino is anomalously small compared with the masses of other particles. There are some reasonably convincing explanations for a small neutrino mass. The smallness may be associated with a small lepton number violation. That is, the neutrino mass is controlled by a Majorana mass term rather that the Dirac mass term, which is responsible for the mass of other particles. So a first question to ask is whether the neutrino is a Dirac or Majorana particle. Another important issue is generation mixing. We must also ask if the massive neutrino is stable or not. CP violation in the lepton sector might be substantially different from what we can see in the quark sector. All these questions may be closely related to the physics at a very high energy, much higher than the present experiments can explore.

The dominant part of the current experimental effort with neutrinos is concerned with the search for a finite neutrino mass. The most straightforward approach is the search for the neutrino mass with nuclear beta decay.

One possible method is based on the bolometric technique.[21] The energy released by particles in dielectric diamagnetic crystals gives rise to a measurable variation of temperature with respect to the working temperature ($T \sim 10$ mK). One of the best candidates to search for double beta decay is ^{130}Te due to its high transition energy ($Q_{\beta\beta} = 2528.8 \pm 1.3$ keV) and large isotopic abundance (33.8%). This last property allows for a sensitive experiment to be performed with natural tellurium. To also achieve good thermal and mechanical properties one can choose TeO_2 single crystals.

The CUORICINO detector is a tower-like structure made by eleven planes (modules of 4-large TeO_2 crystals, $5 \times 5 \times 5$ cm^3, 790 g each) and two planes (modules) of nine small TeO_2 crystals, $3 \times 3 \times 6$ cm^3, 330 g each).[21] All crystals are made of natural tellurium with the exception of 4 small ones which are isotopically enriched. The total mass of TeO_2 of the CUORICINO detector is 40.7 kg, which contains 11 kg of ^{130}Te.

Accumulation of experimental information for the $2\nu\beta\beta$ processes (transitions to the ground and to excited states) yields a better understanding of the nuclear part of double beta decay in general and allows one to check theoretical schemes of nuclear matrix elements for the two-neutrino mode as well as for the neutrinoless one.

Due to the strong energy dependence of the double-beta decay probabilities, the search for such transitions to excited states is not always possible. For isotopes with high decay energies, $Q_{\beta\beta}$, the half-lives of the $2\nu\beta\beta$-decay to the 0^+ level in the daugther nucleus could be of the order of $(10^{20} - 10^{22})$y so the process might be detected using the available low-background detectors.

We see that for ^{130}Te, and the CUORICINO experiment, these conditions are satisfied. The purpose of this work is to put a best bound, or measure the half life of the $2\nu\beta\beta$-decay of ^{130}Te into first excited state 0^+ of ^{130}Xe.

Chapter 1

Introduction

1.1 Neutrinos

In 1930 W. Pauli postulated the existence of the neutrino in order that the energy conservation law in the nuclear beta-decay process to be satisfied. In this reaction the emitted electron exhibits a continuous energy spectrum,[8,21,26,31,34] Pauli considered the neutrino as being electrically neutral (to ensure the conservation of the electric charge) and having the spin $1/2$ (for the conservation of the angular momentum). He expected that the mass of the neutrino would be small, but not necessary zero. Pauli argued that this particle may have a finite, but small, magnetic moment no greater than 0.02 Bohr magnetons and with a penetration power of at least 10 times greater than that of the gamma ray.

Using Pauli's idea, E. Fermi in 1934 proposed his famous theory of the beta-decay. Other neutrinos were experimentally discovered: the muon neutrino and the tau neutrino (associated with the respective leptons: μ and τ). In the same year, 1934, Bethe and Critchfield described the role of β-decay in thermonuclear reaction chains powering the stars,[18]

$$(A, Z) \rightarrow (A, Z-1) + e^{+} + \nu_e, \tag{1.1}$$

thus predicting that the sun produces an enormous neutrino flux.

In 1952 Pontecorvo discussed the possibility of the neutrino oscillations, and later in

1962, Maki and Pontecorvo in 1967 proposed the concept of "mixing" between different flavors of neutrinos.

The most striking advance in our understanding neutrinos was the discovery of parity violation.[18] If they were Dirac particles with absolutely no mass, neutrinos would violate parity because their spins would always aligned along the direction of motion, while the spins of antineutrinos would point the opposite way. Neutrinos have left-handed chirality and antineutrinos are right-handed. Much experimental evidence pointed to the introduction of this concept of parity non-conservation in the weak interactions (Lee and Yang in 1956). This was followed by the Standard Model (Glashow 1961, Salam 1968, Weinberg 1967), which unifies the electromagnetic and weak interactions. The observation of the weak neutral currents and the discovery of the intermediate vector bosons, $W^{\pm}$ and Z^0, guaranteed the success of the model. But the Standard Model needs to be extended and generalized.

The existence of the neutrino was confirmed by Reines and Cowan[31] in 1956 using an antineutrino flux from a nuclear reactor, detecting $p+\bar{\nu} \rightarrow n+e^+$ followed by $e^+e^- \rightarrow \gamma\gamma$ and a γ ray emitted from neutron capture on Cd in a large organic scintillator.[18] The fact that the neutrino from the beta-decay is left-handed $(V - A)$ was confirmed by an (e, ν) angular correlation with ^{135}A with a devised experiment which measured the γ circular polarization emitted from the excited state of ^{152}Sm in the electron capture of ^{152}Eu.[19]

Neutrinos are also important in the astrophysical environment.[31] They are produced in large quantities in a high-temperature and/or high density environment, and these neutrinos may often be used to probe some of their properties which can by no means be accesible by laboratory experiments. The representative examples are the neutrino mass limit from the cosmological mass density of the universe, and the solar neutrino problem.

The recent results from the neutrino oscillation experiments showed that neutrinos have finite mass.[23] However, in such experiments only the difference between the square of the neutrino mass eigenvalues can be measured, and only a lower limit on the absolute mass scale can be obtained in this way (see Figure 1.1). Neutrino oscillation experiments can only provide data on the mass differences of the neutrino mass-eigenstates. The absolute scale can only be obtained from direct mass measurements, ^3H end-point measurements or, in the case of Majorana neutrinos, more sensitively by neutrinoless double-beta decay. This is the reason that the double beta-decay experiments are so appealing. These experiments have already a sensitivity corresponding to the mass scale indicated by neutrino oscillation experiments. If the mass scale is below ~ 0.20 *eV*, $\beta\beta$ -decay may be the only hope for measuring it.

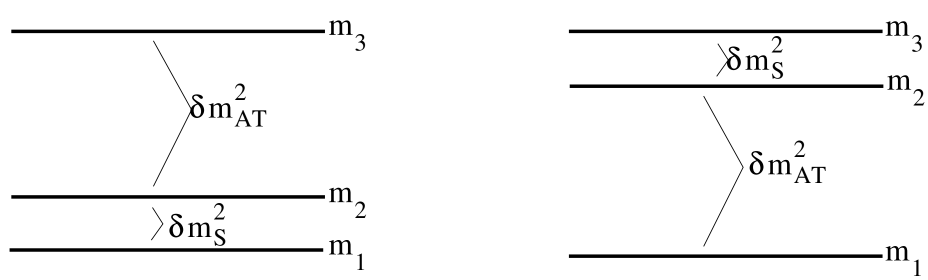

Figure 1.1: Normal and inverted mass hierarchies schemes. Quasi-degenerate hierarchy corresponds to the case $m_1 \gg \delta m_{AT} \gg \delta m_S$

If the neutrinos are massive, the question, are they Dirac or Majorana particles, becomes fundamental.[20] In the Dirac description of spin $1/2$ fermions (Dirac particle), there exist the negative energy states which lead to the symmetric description of particles and antiparticles. In 1937, Majorana showed that it is possible to construct the theory using the real representation of the classical spinor field, which is called the Majorana field. In this scheme, the particle is assigned to be equal to its antiparticle and four degrees of freedom of one Dirac particle are reduced to two, i.e., two spin states. Therefore, the Majorana scheme can be used to describe neutral fermions such as neutrinos. In the gauge theories with both left- and right-handed weak interactions, if neutrinos are massless, there is no distinction between Majorana and Weyl (Dirac) descriptions because the left- and right-handed neutrinos represent the independent degrees of freedom. The difference between Dirac and

Majorana particles is related to the transformation property with respect to charge conjugation. As far as we know, the neutrinos interact only weakly and this type of interaction is not invariant with respect to charge conjugation.[18] As a consequence, a Majorana neutrino in interaction cannot be an eigenstate under the charge conjugation operation, C, because if a Majorana neutrino has a definite value, C, at some instant of time, it will not not have it at some succesive moment because the weak interaction is interchanging the eigenstates. For this reason we have to generalize the definition of the Majorana particle and include also the transformations with respect to other discrete symmetries like the parity, P, and the time reversal, T, (or combinations of them, CP or CPT). The interactions should involve neutrino states of given chirality (left-handed or right-handed) and the formalism should be based on the chiral projections of the corresponding states.

We need to understand why the observed left-handed electron neutrinos are so light, even though in the Standard Model they are treated similarly to quarks and charged leptons. One idea is the so-called "see-saw" mechanism, proposed by Gell-Mann, Ramond and Slansky and by Yanagida 1979. In this mechanism, the left- and right-handed Majorana neutrinos can acquire the small and large scall mass separately, instead of forming a Dirac neutrino. From these standpoints, massive neutrinos are likely to be Majorana particles. The idea of the see-saw mechanism to explain the smallness of the electron neutrino mass can be realized in the models which include the $S(2)_L \times SU(2)_R \times U(1)$ guage group. That is, the existence of the right-handed (V+A) current should be confirmed experimentally to utilize the see-saw mechanism.

As for the neutrino mixing, since there exists the Kobayashi-Maskawa (generalized Cabibbo) mixing in the quark sector, it is natural to assume the corresponding neutrino mixing in the letpon sector if neutrinos are massive.

1.2 Double Beta-Decay

The possible existence of $\beta\beta$-decay was first suggestested by Wigner and reported by Goeppert-Mayer in 1935.[33]

Double beta-decay is a rare transition between two nuclei with the same mass number, A, involving a change of the nuclear charge, Z, by two units (converting two neutrons in a nucleus into two protons). Double-beta-decay is a second-order weak interaction, and, consequently, it is one of the slowest processes in the nature, with half-lives normally in excess of 10^{18} years.

The decay can proceed only if the initial nucleus is less bound than the final one, and, in the best candidates, both will be more bound than the intermediate nucleus. Thus, the intermediate nucleus $(A, \pm 1)$ is "situated between" an observable $\beta\beta$ parent (A, Z) and the corresponding $\beta\beta$ daughter $(A, Z \pm 2)$. In the candidates for experimental investigation, we have satisfied:

(a) The single β–decay $(A, Z) \rightarrow$ any state of $(A, Z \pm 1)$ is not possible energetically, or

(b) The single β–decay $(A, Z) \rightarrow (A, \pm 1)$ is possible energetically, for instance to the ground state of $(A, Z \pm 1)$, but is strongly inhibited by an associated large spin change so that the $\beta\beta$–decay $(A, Z) \rightarrow (A, Z \pm 2)$ is actually more probable.

These conditions are fulfilled in nature for the elements given in Table 1.1. Typically, the decay can proceed from the ground state (spin and parity always 0^+) of the initial nucleus to the ground state (also 0^+) of the final nucleus, although the decay into excited states (0^+ or 2^+) is also energetically possible in some cases.[43]

There are different possible modes of the $\beta\beta$–decay, which differ from each other by the light particles accompanying the emission of two electrons.[28] We distinguish between the $\beta\beta$–decay modes depending on whether they proceed with or without lepton-number violation.

The two neutrino double beta-decay ($2\nu\beta\beta$–decay), which involves the emission of two electrons and two antineutrinos (see Figure 1.2 for the Feynman diagram of this decay),

$$(A, Z) \rightarrow (A, Z+2) + 2e^{-} + 2\overline{\nu}_e, \quad (1.2)$$

is a process fully consistent with the standard model (SM) of electroweak interactions, formulated by Glashow, Weinberg, and Salam.[28] In this mode, first considered by Mayer in 1935, the lepton number is conserved.

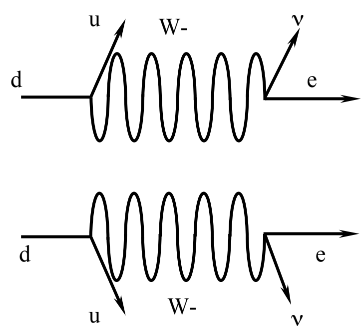

Figure 1.2: Feynman diagram for $2\nu\beta\beta$-decay.

Double-beta-decay, with the emission of a neutrino from one neutron and its absorbtion on another, was first suggested by Furry in 1939. This decay is called the neutrinoless double beta-decay ($0\nu\beta\beta$–decay),

$$(A, Z) \rightarrow (A, Z+2) + 2e^{-} \quad (1.3)$$

This type of decay is expected to occur if lepton-number conservation is not an exact symmetry of nature and thus is forbidden in the SM of electroweak interactions. There is an interesting connection between $\beta\beta$-decay and fundamental particle theory, because $0\nu\beta\beta$-decay can be engendered by Majorana neutrino mass, or explicit right-handed neutrino couplings to hadrons or both. This latter mechanism will produce a vanishing amplitude unless at least one neutrino eigenstate has a non-zero Majorana mass.[9,27] The Feynman diagram describing this decay is presented in Figure 1.3. The standard electroweak model, as well as the minimal $SU(5)$ Grand Unified Theory (GUT), requires neutrinos to be massless. Models which possess left-right symmetry, as well as lepton-hadron symmetry, in general have massive neutrinos. These models are to be probed in $0\nu\beta\beta$-decay experiments. These experiments are probes of physics beyond the Standard Model.

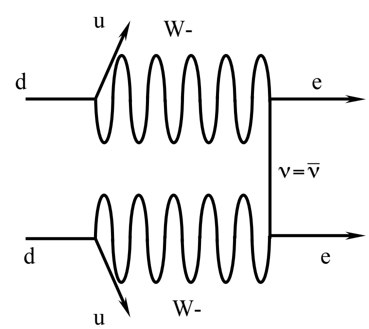

Figure 1.3: Feynman diagram for $0\nu\beta\beta$-decay

Neutrinoless double-beta-decay is actually a very important process both from the particle and nuclear physics point of view, representing a unique tool to establish the absolute neutrino mass scale, its nature (Dirac/Majorana) and the values of the Majorana CP phases. This process can take place only if neutrinos are massive Majorana particles. Unfortunately, uncertainties in the transition nuclear matrix elements still affect the interpretation of the experimental results, and new efforts to overcome this problem are strongly required. Present double beta experiments have reached a sensitivity for $\langle m_\nu \rangle$ in the range 0.2-1.0

eV.[6,50]

If the global symmetry associated with lepton-number conservation is broken spontaneously, the models imply the existence of a physical Nambu-Goldstone boson, called a Majoron,[28] which couples to neutrinos. The Majoron might occur in the Majoron mode of the $0\nu\beta\beta$–decay (Figure 1.4):

$$(A, Z) \rightarrow (A, Z+2) + 2e^{-} + \chi. \tag{1.4}$$

The model of a triplet Majoron was disproved in 1989 by the data on the decay width of the Z^0 boson that were obtained at the LEP accelerator[12] (CERN, Switzerland). Despite this, new models are proposed and this type of decay is possible and where there are no contradictions with the LEP data. There are also other possible mechanisms of $0\nu\beta\beta$–decay induced by lepton-number violating quark-lepton interactions, SUSY extensions of the Standard Model.

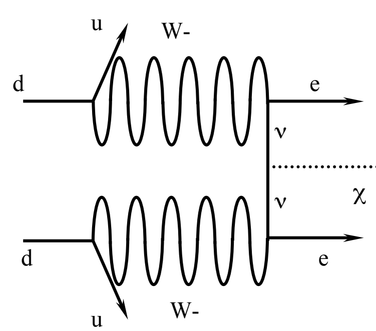

Figure 1.4: Feynman diagram for $0\nu\beta\beta$-decay with the emission of a Majoron χ.

Some nuclear structure calculations imply that there may be a suppression mechanism operative in $2\nu\beta\beta$-decay. In addition, it has been suggested that such suppression mechanisms might extend to $0\nu\beta\beta$-decay. Accordingly, measurements of $2\nu\beta\beta$-decay half-lives can become important and the nuclear physics must be understood if meaningful interpretations are to be made of $0\nu\beta\beta$-decay data. The evaluation methods for the two decay modes showed, however, relevant differences (e.g., the neutrino propagator).[23] An experimental effort to investigate all possible $\beta\beta$-emitters should be addressed.

Experiments which measure, or place limits on, the decay rate w also determine or place limits on the composite neutrino mass $\langle m_\nu \rangle$ or right-handed couplings. The neutrino mass extracted from the experiments is clearly nuclear model dependent.

To extract reliable values or limits on $\langle m_\nu \rangle$ from $\beta\beta$-decay data, it will be necessary to measure the $0\nu\beta\beta$ half life. A signal from the $0\nu\beta\beta$–decay is expected to be a peak at the end of the electron-electron coincidence spectrum as a function of the sum of energies of the two electrons as they carry the full available kinetic energy for this process (see Fig. 1.5). Both, the $2\nu\beta\beta$–decay and the $0\nu\beta\beta\phi$–decay modes yield a continuous electron spectrum, which differ by the position of the maximum as different numbers of light particles are present in the final state.

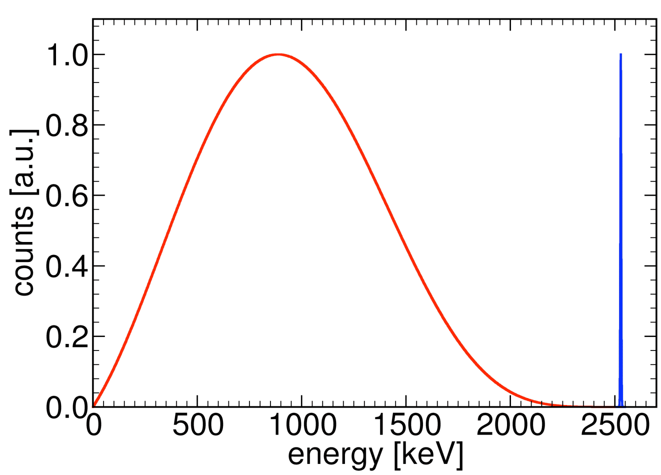

Figure 1.5: Double-beta decay spectrum for ^{130}Te (in red the continuous electron spectrum of $2\nu\beta\beta$–decay; in blue the peak corresponding to $0\nu\beta\beta$–decay)

From a Particle Physics point of view, $0\nu\beta\beta$-decay represents a powerful tool to measure the neutrino Majorana phases and neutrino masses. To determine the very important quantity $\langle m_\nu \rangle$, from the experimental results on $0\nu\beta\beta$-decay lifetime, requires a precise knowledge of the nuclear transition matrix elements. Many, often conflicting, evaluations are available in literature and it is not easy to judge their correctness and accuracy. Good progress has been achieved in this field by the application of the QRPA method and its extensions.[26]

Decay			Q(keV)			Ab.(%)
^{46}Ca	$\rightarrow$	^{46}Ti	987	$\pm$	4.0	0.004
^{48}Ca	$\rightarrow$	^{48}Ti	4271	$\pm$	4.0	0.187
^{70}Zn	$\rightarrow$	^{70}Ge	1001	$\pm$	3.0	0.600
^{76}Ge	$\rightarrow$	^{76}Se	2040	$\pm$	0.9	7.800
^{80}Se	$\rightarrow$	^{80}Kr	130	$\pm$	9.0	50.000
^{82}Se	$\rightarrow$	^{82}Kr	2995	$\pm$	6.0	9.000
^{86}Kr	$\rightarrow$	^{86}Sr	1259	$\pm$	5.0	17.300
^{94}Zr	$\rightarrow$	^{94}Mo	1145	$\pm$	2.5	17.400
^{96}Zr	$\rightarrow$	^{96}Mo	3350	$\pm$	3.0	2.800
^{98}Mo	$\rightarrow$	^{98}Ru	112	$\pm$	7.0	24.100
^{100}Mo	$\rightarrow$	^{100}Ru	3034	$\pm$	6.0	9.600
^{104}Ru	$\rightarrow$	^{104}Pd	1299	$\pm$	2.0	18.600
^{110}Pd	$\rightarrow$	^{110}Cd	2013	$\pm$	19.0	11.700
^{114}Cd	$\rightarrow$	^{114}Sn	534	$\pm$	4.0	28.700
^{116}Cd	$\rightarrow$	^{116}Sn	2802	$\pm$	4.0	7.500
^{122}Sn	$\rightarrow$	^{122}Te	364	$\pm$	4.0	4.600
^{124}Sn	$\rightarrow$	^{124}Te	2288	$\pm$	1.6	5.800
^{128}Te	$\rightarrow$	^{128}Xe	868	$\pm$	4.0	31.700
^{130}Te	$\rightarrow$	^{130}Xe	2528.8	$\pm$	1.3	33.880
^{134}Xe	$\rightarrow$	^{134}Ba	847	$\pm$	10.0	10.400
^{136}Xe	$\rightarrow$	^{136}Ba	2479	$\pm$	8.0	8.900
^{142}Ce	$\rightarrow$	^{142}Nd	1418	$\pm$	2.5	11.100
^{146}Nd	$\rightarrow$	^{146}Sm	56	$\pm$	5.0	17.200
^{148}Nd	$\rightarrow$	^{148}Sm	1928	$\pm$	1.9	5.800
^{150}Nd	$\rightarrow$	^{150}Sm	3367	$\pm$	2.2	5.600
^{154}Sm	$\rightarrow$	^{154}Gd	1252	$\pm$	1.4	22.100
^{160}Gd	$\rightarrow$	^{160}Dy	1729	$\pm$	1.4	21.900
^{170}Er	$\rightarrow$	^{170}Yb	654	$\pm$	1.6	14.900
^{176}Yb	$\rightarrow$	^{176}Hf	1079	$\pm$	2.7	12.700
^{186}W	$\rightarrow$	^{186}Os	490	$\pm$	2.2	26.600
^{192}Os	$\rightarrow$	^{192}Pt	417	$\pm$	4.0	41.000
^{198}Pt	$\rightarrow$	^{198}Hg	1048	$\pm$	4.0	7.200
^{204}Hg	$\rightarrow$	^{204}Pb	416	$\pm$	1.1	6.800
^{232}Th	$\rightarrow$	^{232}U	860	$\pm$	6.0	100.000
^{238}U	$\rightarrow$	^{238}Pu	1146	$\pm$	1.7	99.000

Table 1.1: Double beta-decay candidates

Chapter 2

Theoretical Aspects

2.1 Neutrino Mixing Matrix

Using the Chau and Keung parametrization of the Pontecorvo-Maki-Nakagawa-Sakata (PMNS) neutrino mixing matrix:[22]

$$\begin{pmatrix} \nu_e \\ \nu_\mu \\ \nu_\tau \end{pmatrix} = UV \begin{pmatrix} \nu_1 \\ \nu_2 \\ \nu_3 \end{pmatrix} = \begin{pmatrix} c_3c_2 & s_3c_2 & s_2e^{-i\delta} \\ -s_3c_1 - c_3s_1s_2e^{i\delta} & c_3c_1 - s_3s_1s_2e^{i\delta} & s_1c_2 \\ s_3s_1 - c_3c_1s_2e^{i\delta} & -c_3s_1 - s_3c_1s_2e^{i\delta} & c_1c_2 \end{pmatrix} \times \begin{pmatrix} 1 & 0 & 0 \\ 0 & e^{i\phi_2/2} & 0 \\ 0 & 0 & e^{i(\phi_3/2+\delta)} \end{pmatrix} \begin{pmatrix} \nu_1 \\ \nu_2 \\ \nu_3 \end{pmatrix} \tag{2.1}$$

where $c_i \equiv \cos\theta_i$, $s_i \equiv \sin\theta_i$, V is a diagonal matrix containing Majorana CP phases that do not appear in neutrino oscillations. While this looks very complicated and populated with many unknowns, neutrino oscillation data[1,2,4,5,24,36,45] have constrained all three of the angles and squared neutrino mass differences as shown in Table 2.1.

Considering the values found in Table 2.1, we find it is possible to make the approximation that $\theta_2 \equiv 0$ and assume maximal mixing for the atmospheric neutrino oscillation

Parameter	Best fit	3σ
δm^2_{21} $[10^{-5}eV^2]$	6.9	5.4–9.5
δm^2_{32} $[10^{-3}eV^2]$	2.6	1.4–3.7
$\sin^2\theta_1$	0.52 0.31–0.72	
$\sin^2\theta_2$	0.006	$\leq$ 0.054
$\sin^2\theta_3$	0.30 0.23–0.39	

Table 2.1: Best-fit values and 3σ intervals for the three-flavour neutrino oscillation parameters from global data including solar (SK and SNO), atmospheric (SK and MACRO), reactor (KamLAND and CHOOZ) and accelerator (K2K) experiments[38] ($\delta m^2_{ij} = m^2_i - m^2_j$).

data, or $\theta_1 \cong 45°$. Accordingly,

$$U \cong \begin{pmatrix} c_3 & s_3 & 0 \\ -s_3c_1 & c_3c_1 & s_1 \\ s_3s_1 & -c_3s_1 & c_1 \end{pmatrix} \cong \begin{pmatrix} \frac{\sqrt{3}}{2} & \frac{1}{2} & 0 \\ -\frac{1}{2\sqrt{2}} & \frac{\sqrt{3}}{2\sqrt{2}} & \frac{1}{\sqrt{2}} \\ \frac{1}{2\sqrt{2}} & -\frac{\sqrt{3}}{2\sqrt{2}} & \frac{1}{\sqrt{2}} \end{pmatrix} \tag{2.2}$$

where $c_3 = \frac{\sqrt{3}}{2}$, $s_3 = \frac{1}{2}$ and $c_1 = s_1 = \frac{1}{\sqrt{2}}$ were used in the second matrix.

2.2 Double Beta Decay

To obtain the formula for the $2\nu\beta\beta$-decay rate, we use the standard allowed approximation and assume that Gamow-Teller transition dominates over Fermi transition in medium-mass and heavy nuclei.[20,26,27] The inverse half life of the $2\nu\beta\beta$ decay connecting the 0^+ ground states of two even-even nuclei is then given by the formula

$$\left[T^{2\nu}_{1/2}\left(0^+_i \to 0^+_f\right)\right]^{-1} = G^{2\nu}(E_{max}, Z)|M^{2\nu}_{GT}|^2, \tag{2.3}$$

where

$$M^{2\nu}_{GT} = \sum_m \frac{\langle 0^+_f \,|\sum_l \sigma(l)\tau^+(l)|\, 1^+_m\rangle\langle 1^+_m \,|\sum_k \sigma(k)\tau^+(k)|\, 0^+_i\rangle}{E_m - (M_i + M_f)/2}. \tag{2.4}$$

Here, $|0_i^+\rangle$ ($|0_f^+\rangle$) is the 0^+ ground state of the initial (final) nucleus with mass M_i (M_f); $1_m^+\rangle$ are the 1^+ states in the intermediate odd-odd nucleus with energies E_m. $\sigma(l)$ are the Pauli spin operators for the lth nucleon and $\tau^+(l)$ is the isospin raising operator changing a neutron into a proton. We use the normalization $\langle p|\tau^+|n\rangle = 1$. The function $G^{2\nu}(E_{max}, Z)$ results from integration over lepton phase space. This function has been calculated by Doi *et al.*[20,27]

In the $0\nu\beta\beta$-decay case, one is justified in neglecting the variation of the energy denominator with nucelar excitations and in performing the summation over the intermediate states by closure. The neutrino propagation is characterized by the function $H(\bar{E}, r)$ ("neutrino potential"),

$$H(\bar{E}, r)\frac{1}{4\pi^2}\int d^3k \frac{e^{i\boldsymbol{k}\cdot\boldsymbol{r}}}{k(k+\bar{E})} = \frac{\Phi(\bar{E}r)}{r}, \tag{2.5}$$

where $\bar{E} = \langle E\rangle - (M_i + M_f)/2$ and $\langle E\rangle$ is the "typical" excitation energy of the intermediate nucelus. The function $\Phi(x) \simeq e^{-1.5x}$. With these approximations we can write the inverse half-life for $0\nu\beta\beta$-decay in the form

$$\left[T_{1/2}^{0\nu}\left(0^+ \to 0^+\right)\right]^{-1} = G^{0\nu}(E_{max}, Z)\left|M_{GT}^{0\nu} - \frac{g_V^2}{g_A^2}M_F^{0\nu}\right|^2 \langle m_\nu\rangle^2, \tag{2.6}$$

where the $0\nu\beta\beta$ Gamow-Teller and Fermi matrix elements are given by

$$M^{0\nu} = \left\langle 0_f^+ \left| R\sum_{k,l} K(k,l)\sigma(k)\cdot\sigma(l)\tau^+(k)\tau^+(l)\right| 0_i^+\right\rangle$$

$$M_F^{0\nu} = \left\langle 0_f^+ \left| R\sum_{k,l} K(k,l)\tau^+(k)\tau^+(l)\right| 0_i^+\right\rangle \tag{2.7}$$

$$K(k,l) = H\left(\bar{E}, |r(k) - r(l)\right).$$

The sumation on (2.7) is over all pairs of nucleons k, l with relative vector $r(k) - r(l)$. The function $G^{0\nu}$ results from integration over leptonic phase space.

The quantity $|\langle m_\nu \rangle|$ is the effective Majorana electron neutrino mass given by:

$$|\langle m_\nu \rangle| \equiv ||U_{e1}^L|^2 m_1 + |U_{e2}^L|^2 m_2 e^{i\phi_2} + |U_{e3}^L|^2 m_3 e^{i\phi_3}|, \tag{2.8}$$

where $e^{i\phi_2}$ and $e^{i\phi_3}$ are the Majorana CP phases (± 1 for CP conservation) and $m_{1,2,3}$ are the mass eigenvalues. The measured values of δm_{21}^2 (δm_S^2 solar) and δm_{32}^2 (δm_{AT}^2 atmospheric) given in Table 2.1 motivate the pattern of masses in two possible hierarchy schemes shown in Figure 1.1.

The effective Majorana neutrino mass, $|\langle m_\nu \rangle|$, is directly derivable from the measured half-life of the decay as follows:

$$|\langle m_\nu \rangle| = m_e \, \frac{1}{\sqrt{F_N \, \tau_{1/2}^{0\nu}}} \;\; [\text{eV}], \tag{2.9}$$

where $F_N \equiv G^{0\nu} \, |M_{GT}^{0\nu} - (g_V/g_A)^2 \, M_{GT}^{0\nu}|^2$. This quantity is derived from nuclear structure calculations and is model dependent.

In the case of inverted hierarchy the correct expression for $|\langle m_\nu \rangle|$ can be obtained by interchanging the first and third columns of UV, i.e. by interchanging the roles of m_1 and m_3.

In general, prior to the approximation $\theta_2 = 0 = s_2$, in the normal hierarchy case we have:

$$|\langle m_\nu \rangle|_{NH} = |c_3^2 c_2^2 m_1 + s_3^2 c_2^2 e^{i\phi_2} m_2 + s_2^2 e^{i\phi_3} m_3|. \tag{2.10}$$

while in the inverted hierarchy we have:

$$|\langle m_\nu \rangle|_{IH} = |s_2^2 e^{i\phi_3} m_1 + s_3^2 c_2^2 e^{i\phi_2} m_2 + c_3^2 c_2^2 m_3|. \tag{2.11}$$

With the values and errors (3σ) from Table 2.1, these becomes

$$|\langle m_\nu \rangle|_{NH} = |(0.69^{+0.04}_{-0.11})m_1 + (0.30^{+0.07}_{-0.08})e^{i\phi_2}m_2 + (< 0.054)e^{i\phi_3}m_3|. \qquad (2.12)$$

and,

$$|\langle m_\nu \rangle|_{IH} = |(< 0.054)e^{i\phi_3}m_1 + (0.30^{+0.07}_{-0.08})e^{i\phi_2}m_2 + (0.69^{+0.04}_{-0.11})m_3|. \qquad (2.13)$$

From the relations in Figure 1.1, we can write

$$m_2 = \sqrt{\delta m_S^2 + m_1^2}$$

and

$$m_3 = \sqrt{\delta m_{AT}^2 + \delta m_S^2 + m_1^2}$$

in the case of normal hierarchy and

$$m_2 = \sqrt{\delta m_{AT}^2 + m_1^2}$$

and

$$m_3 = \sqrt{\delta m_S^2 + \delta m_{AT}^2 + m_1^2}$$

in the case of inverted hierarchy. Equations (2.10) and (2.11) can be therefore expressed in terms of mixing angles, δm_S^2, δm_{AT}^2, and CP phases as follows:[15,40]

$$|\langle m_\nu \rangle|_{NH} = \left| c_2^2 c_3^2 m_1 + c_2^2 s_3^2 e^{i\phi_2}\sqrt{\delta m_S^2 + m_1^2} + s_2^2 e^{i\phi_3}\sqrt{\delta m_{AT}^2 + \delta m_S^2 + m_1^2} \right| \qquad (2.14)$$

$$|\langle m_\nu \rangle|_{IH} = |s_2^2 e^{i\phi_3} m_1 + s_3^2 c_2^2 e^{i\phi_2}\sqrt{\delta m_{AT}^2 + m_1^2} + c_3^2 c_2^2\sqrt{\delta m_S^2 + \delta m_{AT}^2 + m_1^2}|. \qquad (2.15)$$

With the approximation $\theta_2 \equiv 0$ and the further approximation of $\delta m_S^2 \ll \delta m_{AT}^2$, equations (2.14) and (2.15) are rewritten as follows:

$$|\langle m_\nu \rangle| = m_1 \left| c_3^2 + s_3^2 e^{i\phi_2} \sqrt{1 + \frac{\delta m_s^2}{m_1^2}} \right| \tag{2.16}$$

$$|\langle m_\nu \rangle|_{IH} = \sqrt{\delta m_{AT}^2 + m_1^2} |s_3^2 e^{i\phi_2} + c_3^2|. \tag{2.17}$$

Actual values of $|\langle m_\nu \rangle|$ for different hierarchies have been recently evaluated by many authors on the base of the latest results of neutrino oscillation experiments. The results of the analysis of Pascoli *et al.*, are summarized for reference in Table 2.2.[40]

$\sin^2\theta_3$	$\lvert\langle m_\nu \rangle\rvert^{\max}_{\mathrm{NH}}$	$\lvert\langle m_\nu \rangle\rvert^{\min}_{\mathrm{IH}}$	$\lvert\langle m_\nu \rangle\rvert^{\max}_{\mathrm{IH}}$	$\lvert\langle m_\nu \rangle\rvert^{\min}_{\mathrm{QD}}$
0.0	3.7	8.7	50.6	47.9
0.02	4.6	8.6	49.6	42.8
0.04	5.3	9.9	48.6	45.4

Table 2.2: Present constraints on $|\langle m_\nu \rangle|$. The maximal values of $|\langle m_\nu \rangle|$ (in units of 10^{-3} eV) for the normal (NH) and inverted (IH) hierarchy cases, and the minimal values of $|\langle m_\nu \rangle|$ (in units of 10^{-3} eV) for the IH and QD (quasi-degenerate) cases, for the 90% C.L. allowed values of δm_S, θ_S and δm_{AT}.

The neutrino propagator (2.5), favors small internucleon separations. It is therefore important to include explicitly this short-range nucleon-nucleon correlations created by the "hard-core", which prevents two nucleons from approaching one another too closely. This can be achieved by substituting for K in (2.7) the modified function $\rho K \rho$, with

$$\rho = 1 - e^{-\gamma_1 r^2} \left(1 - \gamma_2 r^2\right), \tag{2.18}$$

therefore suppressing contributions to the radial integral from small nucleon-nucleon separations r. The inclusion of short-range correlations affects the final results appreciably. We have

$$K(k,l) = \rho(r_{k,l}) \frac{e^{-1.5\bar{E}_{k,l}}}{r_{k,l}} \rho(r_{k,l}),$$
$$r_{k,l} = |r(k) - r(l)|\,. \tag{2.19}$$

The $0\nu\beta\beta$-decay represents a unique tool to measure the neutrino Majorana phases and to assess the absolute scale of the neutrino masses. An experimental sensitivity in the range $\langle m_\nu \rangle \sim 10-50$ meV would definitely rule out inverse and quasidegenerate hierarchies thus assessing a direct neutrino mass hierarchy.

2.3 Quasiparticle Random Phase Approximation

As the theoretical tool, the Quasiparticle Random Phase Approximation (QRPA) is used, based on the quasiparticle formalism. The use of quasiparticles makes it possible to include pairing correlations in the nuclear ground state in a simple fashion.[18,26,27] Particle and antiparticle creation and annihilation operators for spherical shell-model states labeled by (jm) are related to each other by the Bogoliubov transformation

$$a^\dagger_{jm} = u_j c^\dagger_{jm} + v_j \tilde{c}_{jm},$$
$$\tilde{a}_{jm} = -v_j c^\dagger + u_j \tilde{c}_{jm}, \tag{2.20}$$

where $\tilde{a}_{jm} = (-1)^{j-m} a_{j-m}$ and $u_j^2 + v_j^2 = 1$. The vacuum of the quasiparticle operators c and $c^\dagger$ (the BCS ground state) is denoted $|0\rangle$.

The goal is to calculate transition amplitudes associated with charge changing, but otherwise as yet unspecified, one-body transition operators T^{JM} connecting the 0^+ ground state of an even-even nucelus with any of the J^π excited states of the neighboring odd-odd nuclei. Assuming the nuclear motion to be harmonic, we describe the excited states of the odd-odd nuclei by the solutions of the QRPA eigenvalue equation

$$\begin{pmatrix} A & B \\ -B & -A \end{pmatrix} \begin{pmatrix} X \\ Y \end{pmatrix} = \omega \begin{pmatrix} X \\ Y \end{pmatrix}, \tag{2.21}$$

where the matrices A and B are defined as

$$\begin{aligned} A^J_{pn,p'n'} =& \langle 0|(c^\dagger_p c^\dagger_n)^{(JM)\dagger} \hat{H} (c^\dagger_{p'} c^\dagger_{n'})^{(JM)}|0\rangle \\ =& (\tilde{\epsilon}_p + \tilde{\epsilon}_n)\delta_{pn,p'n'} \\ &+ \tilde{V}^J_{pn,p'n'} \left(u_p v_n u_{p'} v_{n'} + v_p u_n v_{p'} u_{n'}\right) \\ &+ V^J_{pn,p'n'} \left(u_p u_n u_{p'} u_{n'} + v_p v_n v_{p'} v_{n'}\right), \end{aligned}$$

and

$$\begin{aligned} B^J_{pn,p'n'} =& \langle 0|\hat{H}(c^\dagger_p c^\dagger_n)^{(J-M)}(-)^M (c^\dagger_{p'} c^\dagger_{n'})^{(JM)}|0\rangle \\ =& (-)^J \Big[\tilde{V}^J_{pn,p'n'} \left(v_p u_n u_{p'} v_{n'} + u_p v_n v_{p'} u_{n'}\right) \\ &- V^J_{pn,p'n'} \left(u_p u_n v_{p'} v_{n'} + v_p v_n u_{p'} u_{n'}\right)\Big]. \end{aligned}$$

Here, $\tilde{\epsilon}$ are the quasiparticle energies obtained by solving the BCS equation for the nuclear

Hamiltonian $\hat{H}$. The operator

$$(c_p^\dagger c_n^\dagger)^{(JM)} = \sum_{m_p,m_n} \langle j_p m_p j_n m_n | JM \rangle c^\dagger_{j_p m_p} c^\dagger_{j_n m_n}$$

creates a proton and a neutron quasiparticle coupled to total angular momentum J and projection M, $X = X^J_{pn}(m)$ and $Y = Y^J_{pn}(m)$ are the forward and backward QRPA amplitudes.

The quantities $\tilde{V}^J$ and V^J are two-body matrix elements of the nucleon-nucleon interaction $\hat{V}$. The former corresponds to the particle-hole part of the neutron-proton interaction, and the latter to the particle-particle part.

Finally, we obtain a generic matrix element of the form

$$M \equiv \sum_{pn,p'n'} Z^J_{pn,p'n'}(m) \left[u_p v_n Y^J_{pn}(m) + v_p u_n (-)^J X^J_{pn}(m)\right]$$
$$\times \left[u_{p'} v_{p'} X^J_{p'n'}(m) + v_{p'} u_{n'} (-)^J Y^J_{p'n'}(m)\right], \tag{2.22}$$

where u, v, X and Y are the BCS occupation amplitudes and QRPA solutions for the initial nucleus, or for the final nucleus. The different decay modes are described by different forms of the coefficient Z, which is given by

$$Z^J_{pn,p'n'}(m) = \delta_{J,1} \frac{\langle p || \sigma\tau^+ || n \rangle \langle p' || \sigma\tau^+ || n' \rangle}{\omega(m) - (M_i + M_f)/2}, \tag{2.23}$$

for the $2\nu\beta\beta$ Gamow-Teller mode $(M^{2\nu}_{GT})$, and by

$$Z^J_{pn,p'n'} = (2J+1) \sum_{J'} \sqrt{2J'+1} (-)^{j_p + j_{n'} + J'} W(j_p j_n j_{n'} j_{p'}; JJ')$$
$$\times \langle (j_p(1) j_{p'}(2))^{(J')} || RK(1,2) \sigma(1) \cdot \sigma(2) \tau^+(1) \tau^+(2) || (j_n(1) j_{n'}(2))^{(J')} \rangle \tag{2.24}$$

for the neutrinoless Gamow-Teller mode ($M^{0\nu}_{GT}$). The Fermi analog of the latter mode is obtained by omitting the term $\sigma(1) \cdot \sigma(2)$ from the reduced matrix element in (2.24). This method was invented by Vogel *et al.*,.[26,27]

2.4 Double Beta Decay To Excited States

Double beta-decay can proceed through transitions to the ground state as well as to various excited states of the daughter nuclide. Studies of the decays to excited states allow one to obtain supplementary information about double beta decay. During the years the intensive experimental research of the $2\nu\beta\beta$ and $0\nu\beta\beta$ decay transitions to the final ground states produced several half-life values and half-life limits for these processes. More recently a lot of experimental effort has been shifted to measurements of $2\nu\beta\beta$-decay transitions to the excited 0^+ and 2^+ final states. This has been boosted by the rough estimates and calculated results concerning these decays, indicating that the decay to these final states may not be as suppressed as believed earlier. These experiments have lead to new stringent limits on the decay modes and to a genuine half-life value of $T^{(2\nu)}_{1/2} = 6.1^{+1.8}_{-1.1} \times 10^{20}$ yr for the decay of ^{100}Mo to the first excited 0^+ state (0^+_1) in the daughter nucleus ^{100}Ru.[14,46] These results serve as a complementary test for the available nuclear models.

Because of the smaller transition energies, the probabilities for the double beta decay to excited states are substantially suppressed in comparison with transitions to the ground state. Theoretical considerations suggest that decays to the first 2^+ state (2^+_1) seem impossible to be detected in the near future due to the smallness of the associated integrated phase-space factors and angular momentum suppression. To detect decays to the first excited 0^+_1 level of the daughter nucleus we need to use isotopes with high $Q_{\beta\beta}$ values and low background detectors. The half-lives of the $2\nu\beta\beta$-decay to the 0^+_1-level of the daughter nucleus is of the order of $10^{20} - 10^{22}$ years.

For ^{130}Te the Q-value is $Q_{\beta\beta} = 2528.8 \pm 1.3$ keV. The decay scheme is showed in

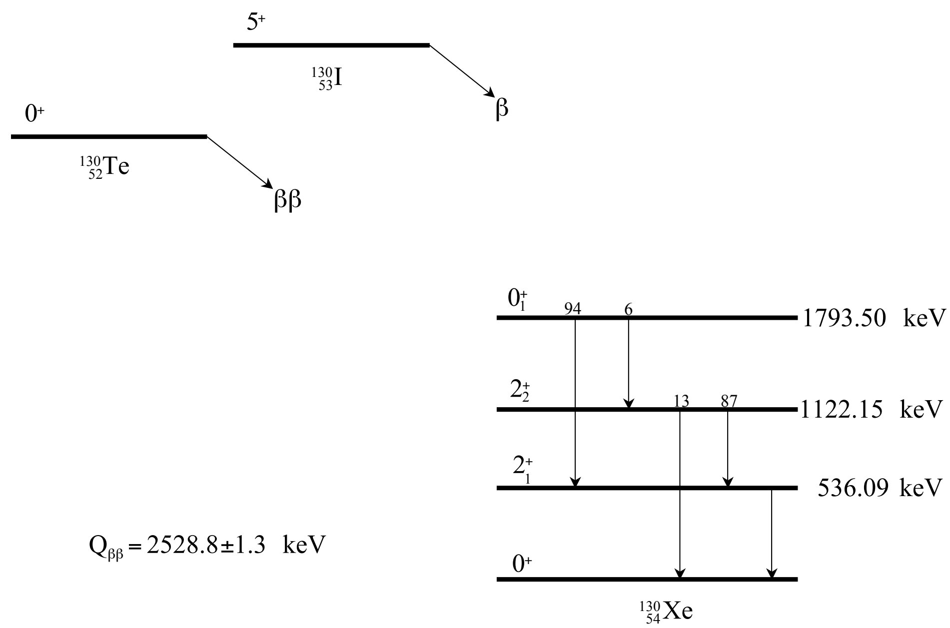

Figure 2.1: Decay scheme of ^{130}Te. Energies of the levels are in keV, and the relative probabilities of γ-rays are in percentages.

Figure 2.1. From this scheme we see that to search for double beta decay to the first excited 0^+ state of ^{130}Xe one should search for coincidences between the two photons that have bigger relative probabilities, namely $E_{\gamma_1} = 1257.41$ keV and $E_{\gamma_2} = 536.09$ keV. The energy of the two electrons, $E_{\beta\beta}$, can take the value from 0 (in fact from the threshold of the detector) up to 735.3 keV.

CUORICINO is a very low background experiments so we can use it to search for this type of decay.

Chapter 3

Bolometric Technique

3.1 Experimental Approach

Experiments on $\beta\beta$-decay can be divided into three categories:[26] geochemical method, radiochemical method and direct counting method.

Double beta decay can be searched for indirectly in radiochemical or geochemical experiments, based on the search of the $(A, Z \pm 2)$ product nuclei.[17,18,43] These experiments are very sensitive but indicate only the presence of the daughter nucleus, and cannot therefore discriminate between lepton conserving and non-conserving processes or between decays to the ground or excited states of the daughter nucleus. In the geochemical method, the $\beta\beta$ decay half life is determined by measuring the abundance of the daughter isotope in an old ore sample containing the parent nucleus. It has an advantage such that the accumulation of decay products (daughter isotopes) for a long period can be used.

The direct counting methods have the ability to discriminate between the $0\nu\beta\beta$-decay mode and the $2\nu\beta\beta$-decay mode, and the $0^+ \rightarrow 0^+$ transition from $0^+ \rightarrow 2^+$ by measuring the energy sum of two electrons and by detecting the γ-ray simultaneously. A common feature of all $\beta\beta$ experiments is the necessity of the reduction of the background[6,9,23] caused mainly by environmental radioactivity, cosmic radiation and residual radioactive contamination of the detector setup elements. Further suppression of background will be the main challenge for future projects whose main goal will be to maximize the $0\nu\beta\beta$-decay rate while minimizing the background contribution.

Direct counting experiments are based on two different approaches. In the first one, the double beta active source is different from detector. This source consists of thin sheets of a double beta decay active material that are inserted in a suitable detector.

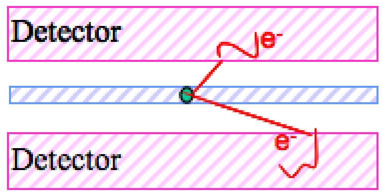

Figure 3.1: Direct counting experiments: source different from detector.

In the second approach, the source and detector coincide. These experiments are known as calorimetric experiments; the detector itself is made of a material containing the double beta decay active nucleus. The use of cryogenic detectors to search for double beta decay was suggested in 1984.[30]

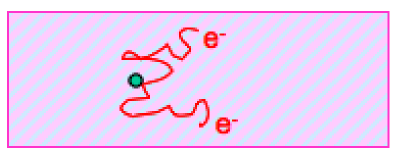

Figure 3.2: Direct counting experiments: source and detector are the same.

3.2 Bolometers

A bolometer is a particle detector that consists of an absorber, which is connected to a heat sink through an insulating link. A sensor is attached to the absorber (see Figure 3.3). With this technique it is possible to obtain information about the characteristics of the interacting particle such as: deposited energy and arrival time. Bolometers have to work at low temperatures because, if not, the thermal fluctuations can hide the particle signals.

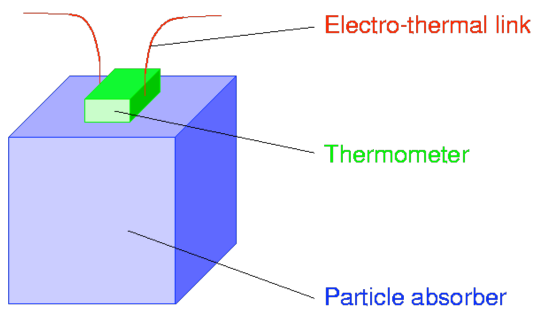

Figure 3.3: Bolometer

Bolometers can be classified according to the type of elementary excitations which mediate the type of elementary interactions. We will consider only bolometers that are sensitive to thermal phonons. These devices are named phonon mediated particle detectors (PMD) and their sensitive element is consequently a phonon sensor.

When a particle interaction occurs in the energy absorber, the phonons produced are out of equilibrium.[41] In fact they have about the Debye energy of the order of tens of meV, while the thermal energy is orders of magnitude lower because of the very low operation temperature. So these phonons are athermal phonons. Normally the athermal phonons degrade their energy and relax onto a new equilibrium distribution by interacting with the surface of the crystal absorber, with the defects of the crystal lattice and with the different isotopes present in the absorber.

According to which type of phonon sensor is used, the PMDs can be fast or slow. In the first case they have a response time of the order of microseconds and can be sensitive to athermal phonons. If the phonon sensor response time is slow and longer than the thermalization time of the non-equilibrium phonons produced by the particle interaction, it will be sensitive mainly to thermal phonons. In the latter case the sensor measures the temperature of the detector and is a thermometer. The PMD works then as a perfect calorimeter. In many experimental situations it is difficult to distinguish between these two extreme cases.

The most important parameter of the detector is the heat capacity that has to be small to achieve large and fast signals. This condition is not very difficult to meet and therefore there is a wide choice for the absorber material.

At low temperatures the specific heat of a crystal can be expressed as

$$c(T) = c_r(T) + c_e(T), \tag{3.1}$$

where c_r represents the lattice contribution to the specific heat and c_e the electron contribution. Dielectric diamagnetic materials are preferred as energy absorbers, as only the lattice contribution is present and, furthermore, it is proportional to the cube of the ratio of temperature and Debye temperature (Debye law) at low temperatures:[30,41]

$$c_r(T) = \frac{12}{5}\pi^4 k_B N_A \left(\frac{T}{\theta_D}\right)^3, \tag{3.2}$$

where k_B, N_A and θ_D are the Boltzmann constant, the Avogadro number and the Debye temperature, respectively. This contribution can be written in terms of heat capacity as

$$C(T) = \beta \frac{m}{M} \left(\frac{T}{\theta_D}\right)^3, \tag{3.3}$$

where $\beta = 1944$ JK^{-1}mol^{-1}, m is the absorber mass, and M is the molecular weight.

In a cryogenic setup this capacity can become so small that even the tiny energy released by a particle in a form of heat generates a measurable temperature increase of the absorber. Cryogenic detectors offer a wide choice of double beta decay candidates, the only requirement being that the candidate nucleus be part of a compound which can be grown in the form of a crystal with the necessary thermal and mechanical properties. The isotope ^{130}Te is an excellent candidate to search for double beta decay due its high transition energy 2528.8 ± 1.3 keV and a large isotopical abundance (33.8%) which allows a sensitive experiment to be performed with natural tellurium.[3,6,7] In addition, the expected signal at 2528.8 keV happens to be in an energy region between the peak and the Compton edge of the ^{208}Tl γ-rays at 2615 keV, which generally dominates the γ background in this high energy region. Of the various compounds of this element, TeO_2 appears to be the most promising one due to its good mechanical and thermal properties.

By thermodynamic considerations, it is possible to express the intrinsic energy resolution ΔE for a bolometric detector sensitive to thermal phonons as:[41]

$$\Delta E = \sqrt{k_B C(T) T^2}, \tag{3.4}$$

where k_B and C are the Boltzmann constant and the energy absorber heat capacity, respectively. For 1 kg of TeO_2 working at 10 mK the intrinsic energy resolution is about 10 eV. We see from (3.3) and (3.4) that the crucial parameter for the energy absorber is its Debye temperature, θ_D, which has to be as high as possible in order to reduce the specific heat.

The other components of the detector are the heat sink and the mechanical and electrical connections (see Figure 3.4):

- The sink bath corresponds to the copper frames of the detector which are in good thermal contact with the coldest part of the dilution refrigerator, the mixing chamber.

- The mechanical holder of the crystal and its main thermal connections to the heat bath are made with teflon (PTFE) pieces. At low temperature PTFE contracts significantly. Therefore, if the teflon pieces are appropriately designed, they could hold the crystals in a safe mode. Furthermore, PTFE is less hard than the copper so it can touch the crystal without breaking it; PTFE is not a good heat conductor at low temperatures. The geometry of the teflon pieces needs to be optimized to obtain the correct termal conductance to the bath. Too low conductances would mean too long thermal pulses; high conductances will result in a loss in signal amplitude because of the energy transfer to the heat bath through the teflon pieces before the temperature reaches its maximum value.

- The electrical contacts are obtained whth gold wires of 25 or 50 μm diameter bounded on the lateral golden sides of the thermistor.

- The coupling between the thermistor and energy absorber is made by some spots of Araldit rapid epoxy deposited on the crystal surface by an array of pins. The height of each spot is $50\,\mu m$.

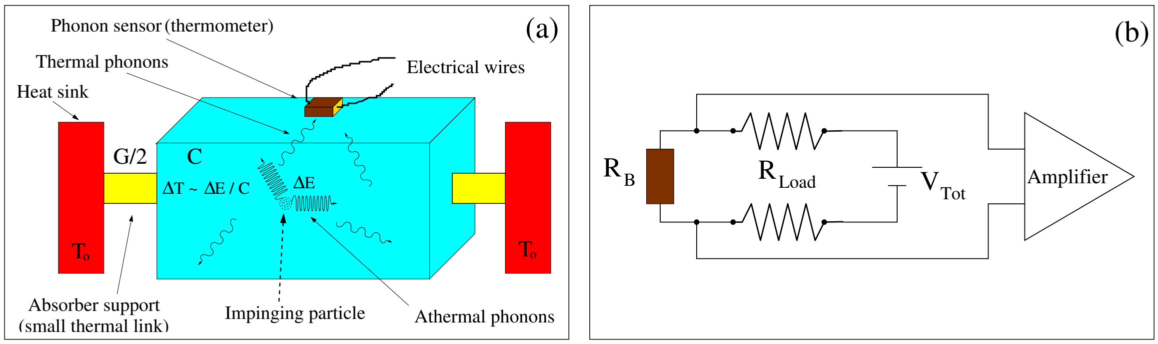

Figure 3.4: Model of the bolometer

It should be remarked that all materials used in the detector construction are to be measured for the level of radioactivity. Only radiopure materials should be used. Copper has the advantage that it has a good heat conductance and that it is relatively easy to obtain batches of copper reasonably clean.

3.3 The Phonon Sensor

In order to achieve a good signal-to-noise ratio, a PMD needs a high sensitivity phonon sensor (thermometer).[41] The phonon sensor is a device that collects the phonons produced in the absorber and generates an electrical signal, proportional to the energy contained in the collected phonons. A simple realization of this device can be accomplished through the use of a thermistor whose resistance, as a function of temperature, has a steep slope. In practice there are two main classes of PMDs which give the best results: semiconductor thermistors (STs) and transition edge sensors (TESs). The value of sensitivity A,

$$A = \left| \frac{d \ln R(T)}{d \ln T} \right| \tag{3.5}$$

is usually in the range 1-10 for STs and in the range 10^2-10^3 for TESs.

The transition edge sensors are superconducting films kept around the critical temperature T_c. They are intrinsically fast and so they can detect athermal phonons. Their working point lies in a narrow range of temperatures. The superconductive film is deposited on the surface of the absorbing crystal. This technique can take advantage of the SQUID (Superconducting Quantum Interference Device) technology as a read-out. TESs are made normally only of a single superconductor, but is possible also to use a bi-layer film formed by a normal metal and a superconductor. In the latter case, because of the proximity effect, the normal metal is driven superconductive and the resulting T_c can be much higher than that of the pure superconductor. In this way it is possible to tune the T_c by adjusting the thickness of the layer.

The semiconductor thermistors (ST) are slow. Their sensitivity is mainly to thermal phonons produced in the absorber. They can give information about systems in thermal equilibrium, and could be considered as temperature sensors. However, it must be remarked that there are clear indications that also athermal phonons can be detected by STs. They consist normally of Ge or Si small crystals with a doped region. A very useful technique for obtaining uniform doped large volumes is the Neutron Transmutation Doping (NTD). In this method, the semiconductor sample is bombarded with neutrons, which induce nuclear reactions on the various isotopes leading to the formation of n- and p-dopants. On the other hand, small low-heat-capacity thermistors can be obtained by ion implantation in Si, using the procedured of the standard Si planar technology.

For both of the previously described approaches, the result is a strong dependence of the sensor resistance with the temperature as follows:

$$\rho \simeq \rho_0 \exp\left(\frac{\epsilon(T)}{k_B T}\right)^{1/2}, \tag{3.6}$$

where k_B is the Boltzmann constant, $\epsilon(T)$ is the activation energy and ρ_0 is a parameter depending on the doping conditions. The conduction mechanism due to dopant sites dominates the conduction at room and lower temperatures. Depending on the number of dopant atoms, the semiconductor at a temperature near absolute zero can behave as an insulator or a metal. So, there exists a critical concentration N_c that characterizes the transition from the insulator to the metallic behavior of the semiconductor. The region near this concentration is called metal-insulator transition region (MIT).[41] At temperatures lower than 10 K, the conduction is due to the migration of charge carriers from an impurity site to another. When the donor concentration is increased, the wave function of the donor atom overlaps with the external electron wave function of the neighboring atoms. In this situation the electrons are not localized and the conduction takes place when electrons jump from one donor site to another (hopping mechanism). The hopping process takes place within the valence band. This migration is due to quantum-mechanical tunneling through the potential barrier which separates the two dopant sites. The conduction is activated by phonon mediation (see Fig. 3.5)

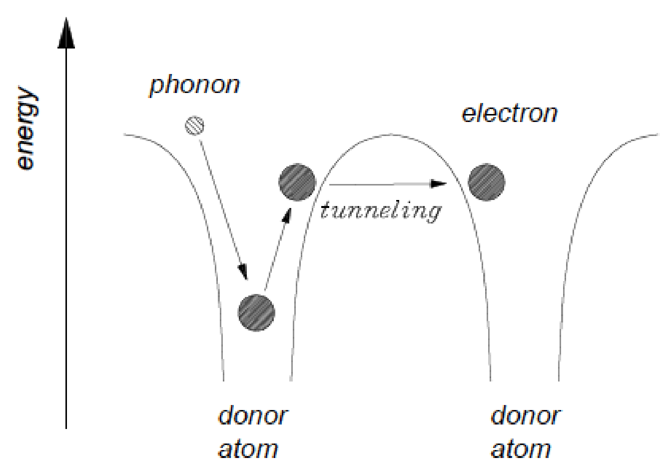

Figure 3.5: Electron hopping mechanism in a semiconductor at temperatures $T < 10$ K

If $T \ll 10$ K, and if the net doping atom concentration is slightly lower than N_c, then the resistivity is strongly dependent on the temeperature. For this reason semiconductor thermistors are operated just slightly below the MIT region. The dominant condction mechanism in this case is called "Variable Range Hopping" (VRH). The carriers can also migrate, in this case, on far sites if their energy levels are located in a narrow range around Fermi energy. As the state density near the Fermi energy in semiconductors is determined by the compensation level K, this level plays a fundamental role in the VRH process, when K is given by:

$$K = \frac{N_A}{N_D}, \tag{3.7}$$

where N_A and N_D are the concentrations of acceptor and donor, respectively. In the VRH region the resistivity depends on the temperature:

$$\rho = \rho_0 \exp\left(\frac{T_0}{T}\right)^{\gamma}, \tag{3.8}$$

where ρ_0 and T_0 are parameters depending on the doping, $|N_D - N_A|$, and compensation levels. The exponent γ is equal to $1/4$ in 3-dimensional Mott model that has low compensation levels (high T). For larger values of K, the Coulomb repulsion among the electrons leads to the formation of a gap (Coulomb gap) in the electron state density near the Fermi energy (low T). The value of γ in this case becomes $1/2$.

The sensor used in a CUORICINO bolometer is a NTD-Ge thermistsor working in the Variable Range Hopping (VRH) conduction regime with Coulomb gap. This kind of thermistor can work as a perfect thermometer and it converts the thermal pulse into an electrical signal using the temperature dependence of its resistivity. The resistance obeys the relation:

$$R = R_0 \exp\left(\frac{T_0}{T}\right)^{\gamma}, \tag{3.9}$$

where $\gamma = 0.5$ just below the MIT region and at a working temperature lower than 1K. A typical resistance vs temperature is presented in Fig. 3.6.

These sensors are realized by neutron transmutation doping of ultra-pure Ge in a nuclear reactor to obtain the proper characteristics of both the resistance and the variation of resistance with temperature.

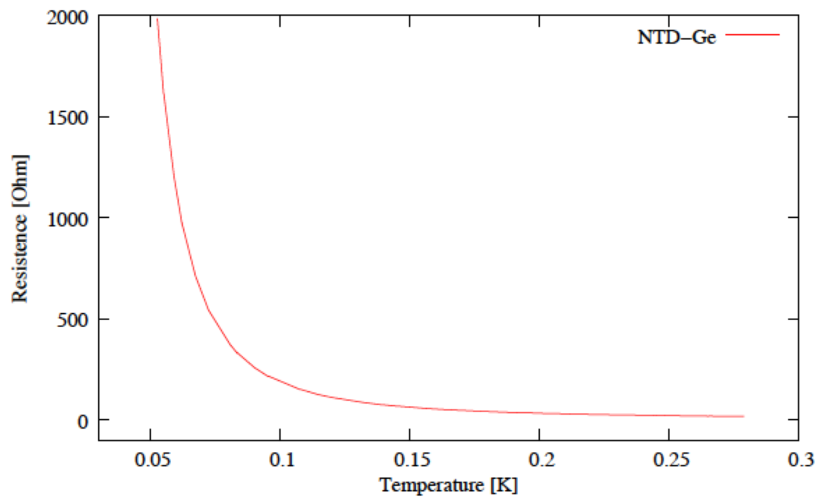

Figure 3.6: Resistance vs. temperature curve for a NTD-Ge thermistor.

Melt-doped Ge crystals cannot achieve the necessary uniformity due to a variety of dopant segregation effects. The only technique for producing such uniformity doping is NTD. In typical aplications, the neutron absorbtion probability for a 3 mm thick wafer of Ge is small, of the order of 3%, leading to a very homogeneous, uniform absorbtion process. The most important aspect of this process is that ^{70}Ge transmutes into Ga, an acceptor, and ^{74}Ge transmutes into As, a donor, the primary active dopant in NTD Ge. In this process, one places the Ge in a nuclear reactor where the following reactions take place:

$$^{70}Ge(21\%) + n \rightarrow {}^{71}Ge(\sigma_T = 3.43 \pm 0.17b, \sigma_R = 1.5b)$$
$$^{71}Ge \rightarrow {}^{71}Ga(t_{1/2} = 11.4 \text{ day}), \qquad \text{Acceptor}$$

$$^{74}Ge(36\%) + n \rightarrow {}^{75}Ge(\sigma_T = 0.51 \pm 0.08b, \sigma_R = 1.0 \pm 0.2b)$$
$$^{75}Ge \rightarrow {}^{75}As(t_{1/2} = 83 \text{ min}), \qquad \text{Donor}$$

$$^{76}Ge(7.4\%) + n \rightarrow\ ^{77}Ge(\sigma_T = 0.16 \pm 0.014b, \sigma_R = 2.0 \pm 0.35b)$$

$$^{77}Ge \rightarrow\ ^{77}Se(t_{1/2} = 38.8 \text{ hours}), \qquad \text{Double Donor}$$

where σ_T and σ_R refer to the thermal and resonance neutron capture cross sections, respectively.

It is very important to optimize the neutron irradiation exposure and to make the exposures as uniform as possible. It is not possible to evaluate the thermistor material directly from the reactor because of the long half life of ^{71}Ge (11.43 days). A delay of several months is required to see if the Ge needs more exposure. To overcome this difficulty, the Ge material is accompanied by calibration foils of metal with long-lived (n, γ) radioactive daughter nuclei. Accordingly, the neutron exposure of the Ge can be determined accurately, and uniformity of exposure is achieved. This technique was developed by the Lawrence Berkeley National Laboratory group. Following the neutron exposure and radioactive decay period, the NTD germanium is first heat treated to repair the crystal structure then cut to obtain strips of the desired geometry.

Chapter 4

Structure and Construction of CUORICINO

4.1 Experimental Details

The CUORICINO detector consists of a tower with 13 planes containing 62 crystals of TeO_2 operating in Hall A of the Laboratori Nazionali del Gran Sasso (LNGS). The main advantage of this type of structure is that each plane of the tower can be considered as an elementary module. Its structure is as follows: the upper 10 planes and the lowest one consist of 4 natural $5 \times 5 \times 5$ cm^3 crystals (44 in total), while the 11th and 12th planes have nine $3 \times 3 \times 6$ cm^3 crystals each (18 crystals). In the $3 \times 3 \times 6$ cm^3 planes the central crystal is fully surrounded by nearest neighbors (see Figure 4.1). The $5 \times 5 \times 5$ cm^3 crystals have a mass of 790 g each and 18 $3 \times 3 \times 6$ cm^3 have a mass of 330 g each.

The small crystals are made with natural tellurium except for four of them. Two are enriched in ^{128}Te and the other two in ^{130}Te, with isotopic abundance of 82.3% and 75%, respectively. The enriched crystals are placed in the corners of the lowest of the 9-crystal modules. Thermal pulses are recorded by means of Neutron Transmitation Doped (NTD)Ge thermistors thermally coupled to each crystal and specifically prepared to present similar thermal performance (see Figure 4.2).

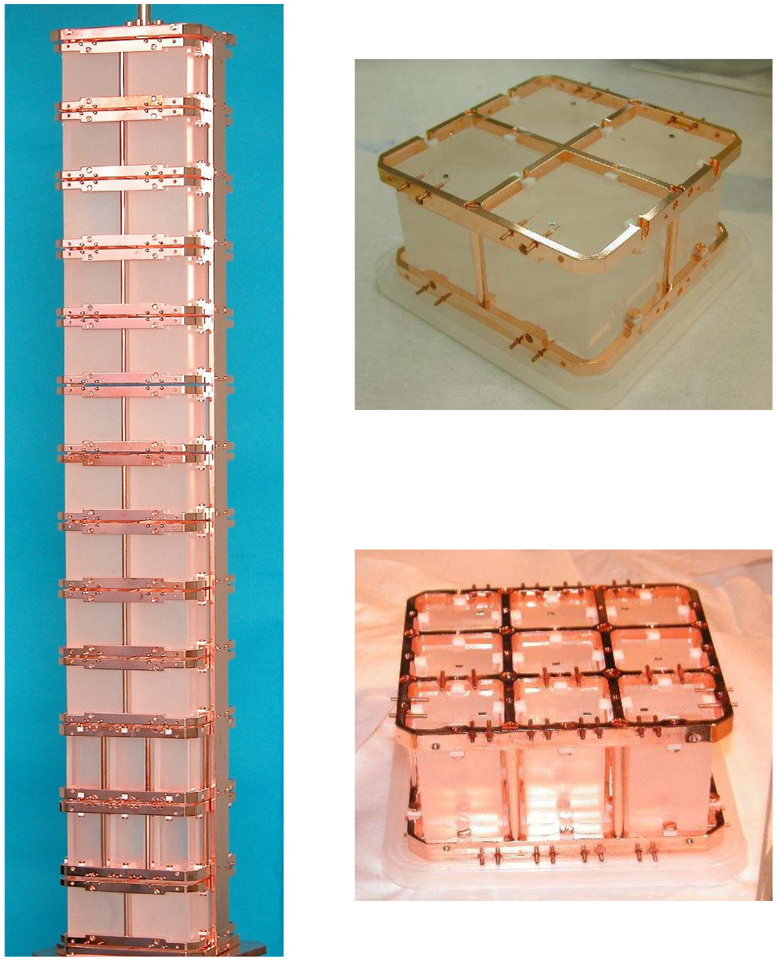

Figure 4.1: CUORICINO tower

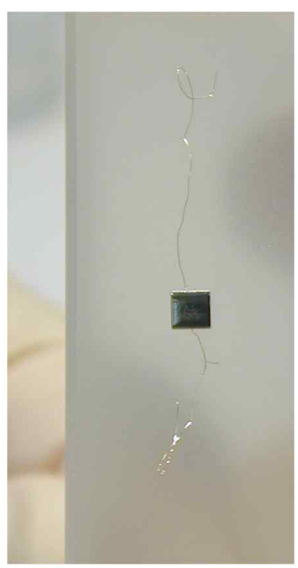

Figure 4.2: NTD Ge thermistor thermally coupled to the crystal

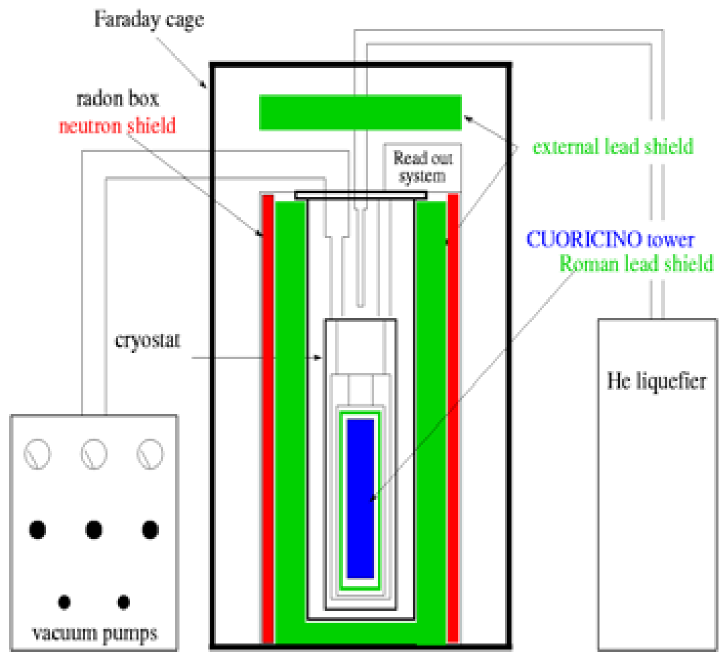

Figure 4.3: Schematic of CUORICINO experiment

The gain of the bolometer is calibrated by means of a resistor of $50-100$ kΩ, attached to each absorber and acting as a heater. The tower is mechanically decoupled from the cryostat in order to avoid vibrations from the overall facility. This reduces the noise in the detectors. The tower is connected through a 25 cm copper bar to a steel spring fixed to the 50 mK plate of the dilution refrigerator (Figure 4.3). The setup is shielded with two layers of lead 10 cm thickness each. The outer one is made of common low-radioactivity lead, while the inner one is made of special lead with a contamination of 16 ± 4 Bq/kg in ^{210}Pb. The electrolytic copper of the refrigerator thermal shields provides an additional shield of 2 cm minimum thickness. An external 10 cm layer of 10% borated polyethylene was installed to reduce the background due to environmental neutrons. In order to shield against the intrinsic radioactive contamination of the dilution unit from the materials used in contruction (e.g., silver and stainless steel) an internal layer of 10 cm of Roman lead (^{210}Pb activity lower than 4 mBq/kg) is located inside the cryostat immediately above the tower of the array. The lateral radioactivity, due mainly to the thermal shields of the dilution refrigerator is reduced by a lateral internal shield of Roman lead of 1.2 cm minimum thickness. The refrigerator is surrounded by a plexiglas anti-radon box flushed with clean N_2 from a liquid nitrogen evaporator, and by a Faraday cage to eliminate electromagnetic interference.

The front-end electronics of all $3 \times 3 \times 6$ cm^3 detectors, and of of 20 of the 44 of the $5 \times 5 \times 5$ cm^3 detectors, are located at room temperature. They consist voltage preamplifiers followed by a second stage and an antialising filter. The differential configuration was adopted to minimize the signal cross-talk and microphonic noise coming from the connecting wires. Precautions have been taken to suppress any possible effect coming from room temperature drift and main power supply instability. A pair of load resistors serves to bias each bolometer in a symmetric way. All the necessary settings for the front-end and the biasing system are programmed remotely via computer, to allow the optimization of the overall dynamic peformance separately for each detector. The so-called cold electronics has been used for the rest of 24 large detectors. In this case the preamplifier is located near the detector (in a box kept at ~ 100 K) to reduce the lenght of the wires and thus the noise due to microphonics which is particularly dangerous in the low energy region of the spectrum, relevant for searches for interactions of WIMPS.

4.2 Gran Sasso National Laboratory

The Gran Sasso National Laboratory (LNGS) in Italy, is the world's largest underground facility for the study of subatomic particles. The laboratory, a 6000-square-meter complex shielded from cosmic radiation by 1400 meters of rock, was built in the mid-1980s alongside a 10-kilometer-long highway tunnel under Gran Sasso Mountain, between Rome and the Adriatic Sea.

The depth of the LNGS (3500 m.w.e) reduces the muon flux down to $\sim 2\times10^{-8}$ cm^{-2}s^{-1}. The muon-induced contribution to the background is therefore expected to be negligible.

Neutrons may constitute a worrisome background for the dark matter experiments be-

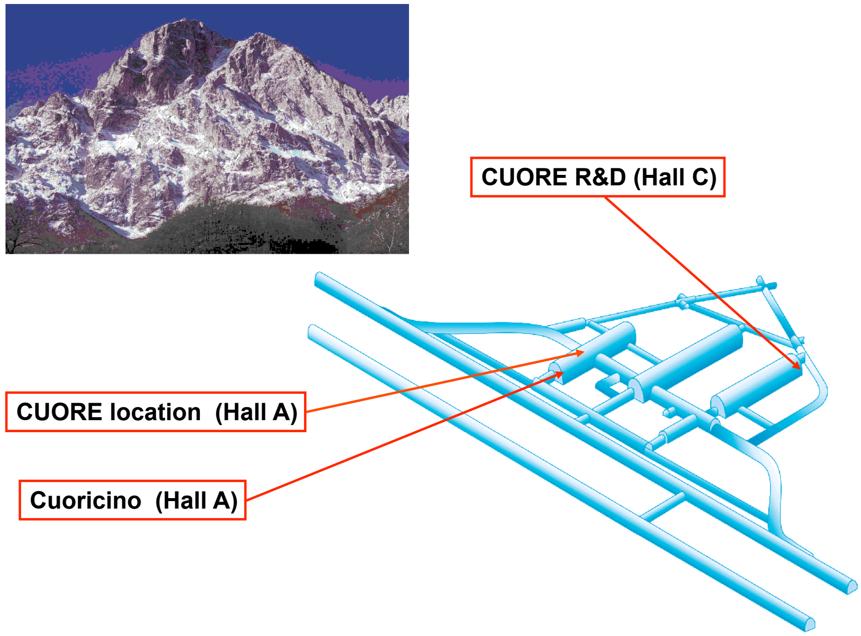

Figure 4.4: Gran Sasso National Laboratory (LNGS), Italy.

cause, for appropriate neutron energies (few MeV), they can produce nuclear recoils ($\lesssim 100$ keV) in the detector target which would mimic WIMP interactions. Simple kinematics implies that in the case of tellurium, neutrons of $1(5)$ MeV could elastically scatter off tellurium nuclei producing recoils of energies up to $31(154)$ keV. In general, one considers neutrons having two origins: from radioactivity in the surroundings or muon-induced. Depending on the overburden of the underground site (i.e., depending on the muon flux), muon-induced neutrons are produced, at lesser or greater rate, both inside and outside the shielding. They are moderated (according to their energies) by the polyethylene/lead shield (when produced outside) or tagged by the muon veto coincidence (when produced within the passive shielding).

In the case of external neutrons (from rocks, from fission processes or from (n, α) reactions, as well as neutrons generated by muons in the walls of the underground site), the environmental neutron flux has been measured in LNGS. The result is $\sim 1 \times 10^{6}$ cm^{-2}s^{-1} for the thermal component, $\sim 2 \times 10^{7}$ cm^{-2}s^{-1} for the epithermal and $\sim 2 \times 10^{-7}$ cm^{-2}s^{-1}

for energies over 2.5 MeV. They are fairly well moderated by the polyethylene and eventually absorbed or captured. At LNGS the muon flux has the value $2.5 \times 10^{-8}\,\mu/(\mathrm{cm}^2\mathrm{s})$. Independent of the mechanism used to reject or tag the events associated to neutrons, their rather small number is expected to play a secondary role in the total background compared with other main sources of background.

A preliminary evaluation of the influence of the environmental γ background in Gran Sasso resulted in a negligible contribution for the $0\nu\beta\beta$ region and a contribution similar to that of bulk contamination of the dark matter region.

4.3 The Treatment Of The Crystal Surfaces

It is very important to use crystal absorbers with low radioactive contamination. A relevant contamination comes from the surface contamination of the crystals. One method to reduce the background level, while maintaining the same quantity of active mass, is to use a larger crystal absorber so that the ratio surface to weight decreases. This is the main reason for using large crystals in the construction of CUORICINO. The crystals were produced by Shanghai Institute of Ceramics (SICCAS). They were grown with pre-tested radioactivity material and shipped to Italy by sea to minimize the activation due to cosmic rays.

To reduce/eliminate the surface contamination introduced by the original production process, the crystals have been lapped with specially selected low contamination abrasives. It was necessary to develop a polishing procedure. After several tests the following procedure was used for all crystals.

1. The first step was used to remove the surface scratches (originating from a first polishing done in China) using $10\,\mu$m Chinese alumina powder. The crystals were lapped 5 minutes on hard surfaces and 3 on soft ones. The thickness of the material removed in this way ranged between 50 and $130\,\mu$m for each face. Unfortunately, the powder was contaminated with U and Th, so the only aim of this step was to obtain

workable crystals for the next phase.

2. The second step represents the real cleaning procedure, whose aim was the removal of surface contamination, including the one possibly introduced during the previous step. We used the $11\,\mu$m radiopure Sumitomo alumina powder and polished the surfaces for $5-8$ minutes, depending on the surface hardness. In this step an ULTRA-PAD (Buehler) cloth was used. ULTRA-PAD is a hard woven aggressive cloth pad for rough grinding, which allows a quick removal of a substantial amount of material. For final polishing a soft LAM 450 (Lamplan) cloth was used for few minutes in order to achieve a better quality of the surface. The amount of material removed in this step was $30 - 45\,\mu$m.

3. The third step was the lapping of the crystal edges for 30 seconds with $11\,\mu$m radiopure Sumitomo alumina powder. This operation did not produced appreciable variations in the weight of the crystals since only a very small quantity of material was removed from the edges.

The cleaning procedure was executed at LNGS in an anti-radon glove box under a saturated atmosphere of pure nitrogen (see Figure 4.5) in a clean room.

Figure 4.5: Anti-radon box inside the CUORICINO clean room, Hall A LNGS Italy

4.4 The Coupling Between NTD-Ge Thermistors And TeO_2 Crystals

Joining a thermistor to the crystal with an homogeneous layer of glue could be a problem due to differential thermal contractions. After some R& D effort[41] a new gluing method to deposit the glue spots on the sensor and not on the crystal. A new tool was designed for this purpose.

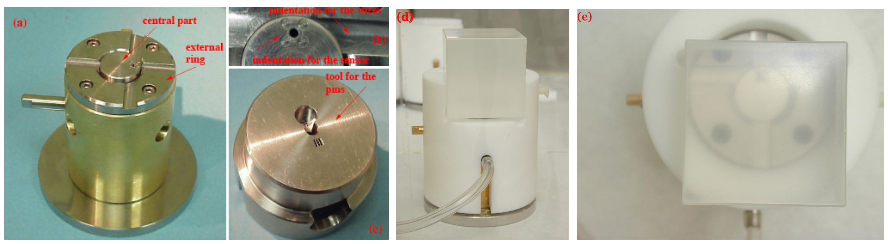

Figure 4.6: The gluing tool used in CUORICINO to attach the sensors to the energy absorbers with glue spots

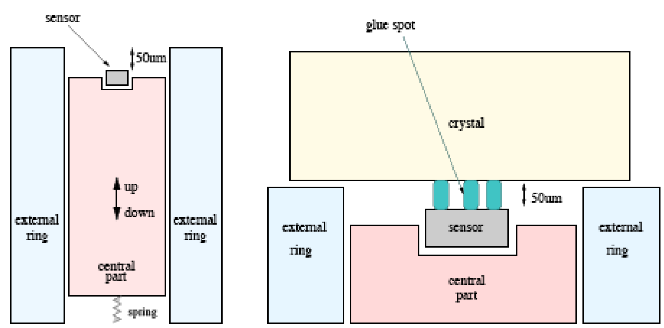

Figure 4.7: The gluing tool used in CUORICINO to attach the sensors to the energy absorbers (schematic drawing)

The gluing procedure was divided in four steps:

- The thermistor was positioned over the indentation in the central part of the gluing tool, paying attention so that also the thermistor gold wires are into the indentations made for them.
- The sensor was arranged in the correct position, i.e., at $50\ \mu$m under the external ring using the specific positioning tool.

Figure 4.8: The gluing process inside the radon-box in the CUORICINO clean room in Hall A at LNGS

- The glue spots were produced on the surface of the thermistor using the cap shown in figure 4.6 (b).

- The TeO_2 crystal was rested on the gluing tool; the bottom of the crystal was touching the external ring of the gluing tool.

4.5 The Array Construction And Setup

The mounting of the TeO_2 crystals is crucial to detector performance, and must fulfil a number of sometimes contradictory criteria:

1. Crystals must be rigidly secured to the frame to prevent power dissipation by friction caused by unavoidable vibrations, that can prevent the crystal from reaching the required temperature and can produce low frequency noise;

2. the thermal conductance to the heat sink (copper frame) must be low enough to delay the re-cooling of the crystal, following a heat pulse, such that the pulse decay time (re-cooling time) is much longer than the rise time;
3. however, the heat conductance must be high enough to guarantee efficient cooling;
4. the frame must compensate for the differences in thermal expansion coefficients of the various materials used;
5. and finally, only materials selected for low radioactivity can be used.

The preparation of the experimental setup was particularly careful in order to select the materials used. The mechanical structure of the array was made exclusively by OFHC copper and Teflon, also radioactive measurements were made before the mounting. The copper has an extremely low radioactive content. Copper and Teflon parts were treated separately with acids to remove any possible surface contamination (Figure 4.9). The pins used in different thermal steps of the refrigerator were removed from their rounded plastic heads because the plastic is radioactive. For the same reason, the connection wires for cold electronics were substituted with new clean ones.

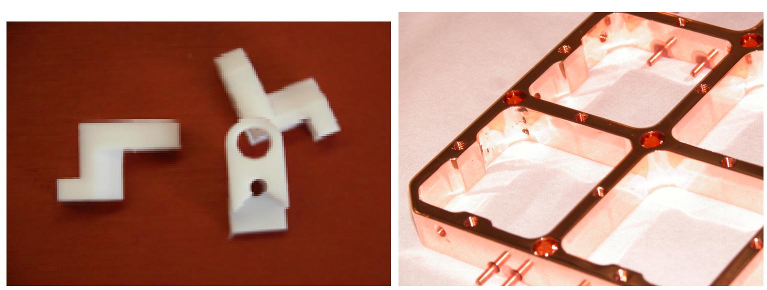

Figure 4.9: Clean Teflon holders. Clean copper frame

The array was finally assembled in an underground clean room having a N_2 atmosphere to avoid Rn contamination (Fig. 4.11).

The array was surrounded by 1 cm thick roman lead shield. Two Roman lead disks, 7.5 and 10 cm thick, are positioned just below and above of the tower, respectively (see Figure

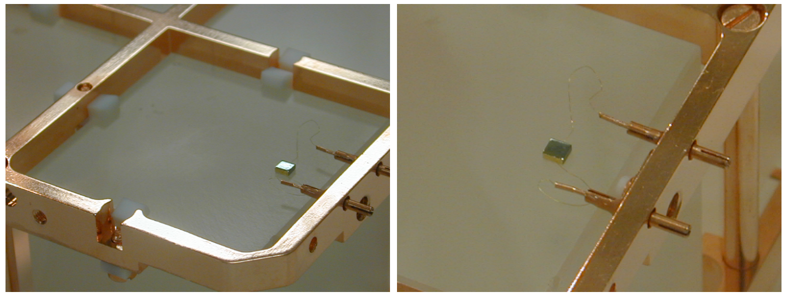

Figure 4.10: Crystal mounted in the copper frame. The wires of the thermistor are also connected

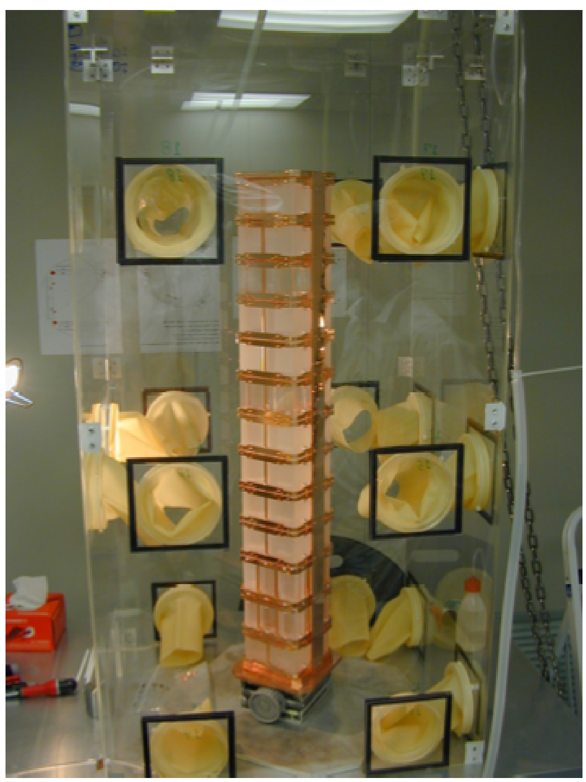

Figure 4.11: Mounting of CUORICINO tower inside a radon box under pure nitrogen atmosphere

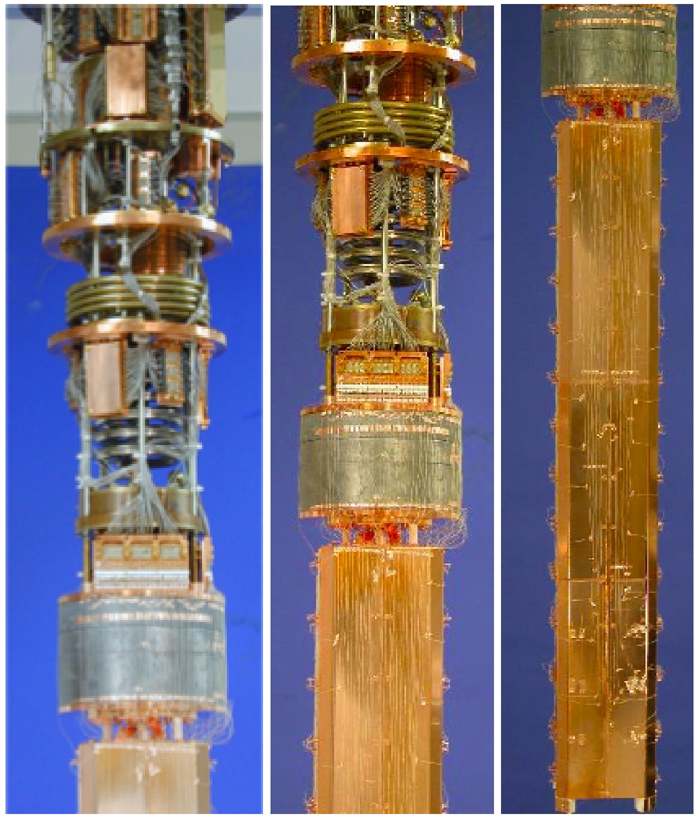

Figure 4.12: CUORICINO tower

4.12). The refrigerator itself is shielded by a 20 cm thick layer of low activity lead and by a 10 cm thick layer of borated PET. Clean nitrogen is flushed continuously between the external lead shield and the cryostat to avoid any Rn contribution to the detector background.

4.6 Data Acquisition System (DAQ)

In CUORICINO, two front-end readouts are used: a configuration consisting of 38 channels completely operated at room temperature (warm electronics) and a system of 24 channels characterized by an additional first differential unity gain buffer stage operated at low temperature (cold electronics).

The connection between the thermistors and the first stage of the electronics is via a twisted pair of 1 m in length for the warm electronics and 5 m in length for cold electronics, respectively. The main reason for these two prototypes is to reduce the effect of the microphonic noise of the connecting wires on the detector energy resolution at low energy, in order to achieve the maximum possible sensitivity at threshold. Since different factors dominate the detector resolution at higher energies, an equivalent performance is obtained there for the two set-ups.

The signals coming from each crystal are amplified and filtered by a preamplifier (see Figure 3.4) that generates pulses well described by the following typical parameters (see Figure 4.13):

- Voltage signals with maximum peak amplitudes as high as 10 V; due to the large energy range, the peak amplitude can also be as low as few mV.
- Rise times of the order of 30 ms, with fall times up to an order of magnitude slower.
- Total duration up to several seconds.

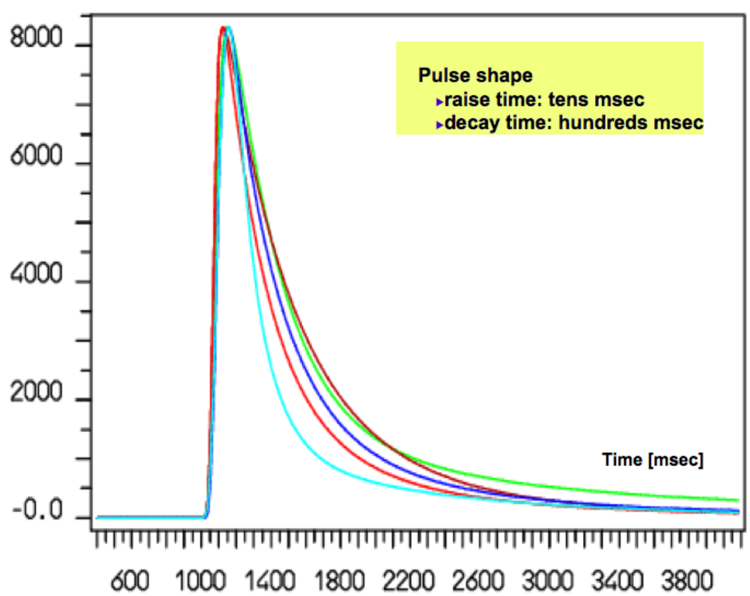

Figure 4.13: Typical pulses coming from crystals

4.7 Heater-Based Stabilization

During a measurement, all the parameters of the detector must be monitored and registered. This is particularly required in long running time cryogenic experiments where many environmental influences can affect the cryogenic apparatus. The experience gained with CUORICINO showed us the fundamental role played by the temperature instabilities and by the vibrations induced by the malfunctioning of the cryostat and liquefier. In order to correlate these frequently unavoidable problems it is very important to continuously check the main parameters of the cryogenic system (e.g. pressures, mixture flows, cryogenic liquid levels and others). In long measurements, one has to cope with fluctuations of liquid bath levels (at 4.2 and 1.5 K) that determine small changes in the flow rate of $^3He -^4 He$ mixture (the working fluid in a dilution refrigerator) that influence the base temperature. The problem can be minimized by directly stabilizing the main cryogenic parameters as much as possible. Therefore we have to stabilize:

- the level of the 1.5 K bath, equating exactly the boil-off to the filling rate regulated by a needle valve,
- the level of the 4.2 main bath, by means of refills,
- in some runs, the mixture flow rate, through a feedback control acting on the still power,
- in some runs, the detector holder temperature, using a heater-thermometer feedback control.

One method of providing the response stabilization is to periodically deliver to each bolometer one or more fixed amounts of energy, generating in the detector a response similar to real events. The injection can be done using Joule pulses delivered by a heater element thermally coupled to the crystal. The general approach is to register the pulse amplitudes, V_p, given by the pulser, together with their arrival times, and then to reconstruct the function $V_p(t)$ which represents the detector response as a function of time. This procedure can be used to correct off-line the amplitudes of every pulse whose arrival time is known. Unfortunately this method has an intrinsic limit. The sampled function $V_p(t)$ is sampled with a certain rate, that canot be too high because it will cause dead time of the detector.

The heater should satisfy the following requirements:[3]

- Its resistance must be reasonably independent of temperature and applied voltage.
- Its heat capacity must be negligible with respect to that of the detector.
- The crystal relaxation time with respect to the developed heat must be shorter than all typical thermal time constants in order to provide an almost instantaneous energy release.
- The mechanism of signal formation for particle interactions and Joule heating must be similar to assure that the pulse amplitude dependences on time, baseline level and other operation conditions, are the same for the two processes.
- the heater resistance must be much bigger than the resistance of the connection wires through the cryostat in order to represent the maine point of power dissipation. For the experimental configuration those values range from 1 kΩ to 10 MΩ.

Steady resistances can be realized either by means of metallic alloys or through a heavily doped semiconductor, well above the metal-insulator transition (MIT), so that a low-mobility metallic behavior is exhibited. The structure must be integrated in a small chip easy to bond and to connect thermally to the crystal.

The heat capacity C_h of the heating element is important for the control of the thermal coupling time τ_h through the formula:

$$\tau_h \simeq \frac{C_h}{G_b}, \tag{4.1}$$

where G_b is the thermal conductance between the heater and detector, and τ_h represents the typical time necessary to achieve thermal equilibrium between heater and detector. Since τ_h should be as small as possible, it is important to reduce the heater heat capacity and to realize good heater-detector thermal coupling.

Doped semiconductor are used as heating elements. The most effective stabilization (gain correction) is based on analyzing the heater signal amplitudes as a function of the base temperature (pulse baseline). The amplitudes of the pulses, V_p, can be correlated with the baseline level V_c immediately preceding the pulse development. V_c can be inspected for every pulse. The relation between pulse amplitude and baseline (bias) level is an intrinsic property of each detector and of its operation point. Once determined with sufficiently high statistics, it can be generally applied for pulse correction.

Chapter 5

Off-Line Analysis

The main goal of the off-line analysis is the extraction of the relevant physics information from the large amount of raw data recorded by the DAQ system.

We can define two levels of analysis. The first level is the pulse analysis. This consists of amplitude evaluation, noise rejection, gain instability and linearity correction. The product of this first level is the production of n-ple's (a proper number of parameters fully describing each bolometric pulse). The second level starts from the n-ple and and its aim is to obtain the physics results (e.g. $\beta\beta(0\nu)$ or Dark Matter interactions). The identification of the background sources is also an important goal of the second-level analysis.

5.1 First-level analysis

When the output voltage of one detector exceeds the trigger threshold, the acquisition system records a number of converted signal samples. The acquired time window (few seconds) must fully contain the pulse development in order to allow an accurate description of its waveform (see Figure 4.13). The existence of a pre-trigger interval just prior to the production of the pulse (baseline) guarantees that a small fraction of the number of acquired samples can be used to measure the DC level of the detector. This voltage can be directly correlated with the detector operating temperature).

For each trigger, an entire waveform is sampled and recorded. The following are important goals for this level of analysis:

1. maximization of the signal to noise ratio for the best estimate of the pulse amplitude; this is accomplished by means of the optimum filter (OF) technique,[32]
2. correction of the effects of system instabilities that change the response function of the detectors (gain stabilization),
3. rejection of the spurious triggered pulses by means of pulse shape analysis,
4. identification and rejection of radioactive background pulses by means of coincidence analysis.

The Optimum Filter (OF) technique is frequently used with bolometers to evaluate the amplitude of a signal superimposed on stochastic noise. This algorithm has proven to provide the best estimate of the pulse amplitude under general conditions. Relative to a simple maximum-minimum algorithm, this technique allows the evaluation of the signal amplitude with much higher efficiency resulting in an effective improvement of the detector energy resolution. The following information is needed to implement the OF technique: the detector response function (i.e. the shape of the signal in a zero noise condition) and the noise power spectrum. Once these are known, the OF transfer function is easily obtained and used as a digital filter for the acquired pulses. The role of the OF transfer function is to weight the frequency components of the signal in order to suppress those frequencies that are highly influenced by noise. The amplitude of the pulse is then evaluated using optimally filtered pulses. Effective pulse-shape parameters can be deduced from the comparison of the filtered pulses with the filtered response function.

The noise power spectrum is periodically evaluated by randomly acquiring a few hundred noise pulses. In order to distinguish actual pulses from random acquired ones induced by microphonic or electronic noise, a pulse shape analysis is performed. Each optimally filtered pulse is compared, after proper normalization, to the optimally filtered reference pulse. The sum of their point-by-point differences is assumed as a shape parameter. Since noise frequencies are suppressed by optimum filter, this parameter is very effective and noise pulses are always fully identified and rejected for energies higher than 50 keV.

In processing the data off-line, the following parameters are evaluated and recorded to disk for each digitized pulse (n-ple):

1. the channel number, i.e., the number of the channel that exceeded the trigger threshold,
2. the absolute time at which the pulse occurred with a precision of 0.1 msec.,
3. the OF amplitude, i.e., the amplitude of the optimally filtered signals,
4. the baseline, obtained by averaging a proper number of points from the pre-trigger interval. Since the detectors are DC coupled, this provides a direct measurement of the detector temperature at the time of the creation of the signal.
5. The signal rise and decay times, are also evaluated as well as,
6. the pulse shape parameters, obtained by comparing the acquired pulse with the expected response function of the bolometer after OF or adaptive filters,
7. the pile-up fraction. Pile-up is usually efficiently rejected by pulse-shape analysis even if this technique can't identify the rejected pile-up events. In order to improve the pile-up rejection and quantitatively evaluate its rate (e.g. for short-time coincidence analysis), the Wiener-filter algorithm is implemented.[42]

The next step is the gain instability correction. The OF amplitudes are corrected to reduce or cancel the effects of system instabilities responsible for the variation of the ratio of the energy E deposited into a given crystal and the amplitude ΔV of the corresponding electrical pulse. There are three instabilities that can modify the ratio $\Delta V/E$ (where

$V = V_b G$ is the output voltage given by the product of the bolometer voltage V_b and the electronics gain G): i) a variation in the electronic gain G, ii) a variation in the bias V_{Tot} and iii) a variation in the temperature T_b of the crystal.

The electronic system is designed to guarantee a stability of G and V_{Tot} within 0.1% . It is however, much more difficult to maintain stability within 0.1% of the detector temperature on long time scales. To overcome this problem, and as already mentioned in previous sections, a silicon resistor glued to each crystal is used as a heater to produce a reference pulse in the detector. It is connected to a high precision programmable pulser that produces a fast voltage pulse every few minutes dissipating the same amount of energy (E_{ref}) into the crystal each time. These voltage pulses mimic pulses produced in the crystal by particle interactions and are used to measure the value of the ratio $\Delta V/E$. Any variation of the amplitude of the reference pulse is due to variations of the $\Delta V/E$ ratio. The OF amplitude of the reference pulse is therefore used to measure the actual value of $\Delta V/E$ every few minutes, while the baseline of the reference pulse provides the contemporary measurement of the value of T. A fit is then used to obtain the values of $\Delta V/E$ as a function of temperature. Therefore, in this step of the off-line analysis, the OF amplitude of each pulse is corrected according to the given value of $\Delta V/E(T[t])$ for the detector temperature at which the pulse has been generated. After correction, these fluctuations were reduced to less than 1 μ K.[3]

Pulse shape analysis is very useful in rejecting spurious signals produced by microphonics and electronic noise. A confidence level is determined for each pulse shape parameter and for the rise and decay time of each pulse. Signals falling within these intervals are defined as “true” (or physical) pulses, while signals having one or more of their parameters outside of the relevant interval are rejected as noise. The use of more than one pulse shape parameter results in better reliability of the rejection technique.

The linearization of the detector response is critically important for energy calibration. The final step in data processing is the conversion of the OF amplitudes into energy values.

The relation between ΔV and E will be obtained periodically by the use of radioactive calibration sources. The ratio $\Delta V/E$ will be measured for several gamma lines, and the data will be fit to the model previously described, but taking into consideration the fact that the thermistor resistance and the crystal heat capacity are temperature dependent. This will provide the calibration function of E as a function of ΔV, that will then be used to convert the OF amplitudes into energy values.

Finally, the close packed array of the crystals will allow the rejection of events that leave energy in more than one crystal. This will be particularly useful in rejecting very high energy gamma rays that enter from outside of the array. The small angle Compton scattering in a single crystal can mimic a double beta decay event, a dark matter scattering, or a solar axion. The probability that this photon would escape the rest of the array without a second interaction is small. In addition, background events from radioactivity within the structure of the array will also have a significant probability of depositing energy in more than one crystal. This will also be true for high and intermediate energy neutrons. In the final stage of off-line analysis, these coincidence events are identified from the data which contain the detector number, signal time, pulse energy, and pile-up parameter.

5.2 Second-level analysis

In the second-level analysis, there are several directions. The main one that coincides with the main goal of CUORICINO is to search for $\beta\beta(0\nu)$ of ^{130}Te . Another direction is to try to identify the radioactive sources that determine the background and eliminate them in the next generation experiment, CUORE. We can also search for $2\nu\beta\beta$ transitions to to excited states. The search for $2\nu\beta\beta$ transitions of ^{130}Te to excited states of ^{130}Xe is the main purpose of this PhD dissertation research.

In this analysis, coincidence and anticoincidence spectra are produced. We need to define a procedure to group the events into coincident events. The histogram of the energies of single events will produce an anticoincidence spectrum and, vice versa, the events that are coincident will produce a coincidence spectrum.

To obtain coincidence events we use the following algorithm. We group the events into disjoint classes; the elements of one class will be considered coincident. Theoretically, two events are in coincidence if the time difference between them is zero. In practice, the time difference can be between 50 ms and 200 ms. Consider a window of time (let us say $\Delta t = 100$ ms). Consider the first event of one n-ple. The time corresponding to it is t_A. We read the following events considering them in coincidence with the first one if their recorded time $t_1, t_2, t_3, \ldots$ satisfies the relation $t_A \leq t_1 \leq t_2 \leq t_3 \leq \ldots \leq t_A + \Delta t$. These events will form class A. Consider the event whose associated time, t_B, is the first one later than $t_A + \Delta t$. This event will determine the beginning of the second window of time and thus the second class. Consider t_i from class A. If $t_i - t_A \leq t_B - t_i$ then we consider that t_i is in class A being coincident with t_A. If we have $t_i - t_A > t_B - t_i$ then we consider that t_i is in class B, thus coincident with t_B. This procedure is repeated, class C being determined by the first event with $t_C \geq t_B + \Delta t$, etc. In this way we put all events in disjoint classes. If an event is alone in a class then that event is obviously a single event. The program using this algorithm will assign to each event in the n-ple, an extra parameter (Class). Events having the same positive value of the Class parameter are in the same class so they are coincident. If the value of class for an event has the value -1, that event is single. In this way is very easy to make an anticoincidence spectrum. We choose only the events in the n-ple having the class parameter equal to -1.

We also need to know if the channels correspond to neighboring crystals. To accomplish this, we defined a new parameter (PositionInTower). Channels having the same value n of this parameter or a value $n \pm 1$ correspond to neighboring crystals. The numbering starts with 1 for the bottom plane and finishes with 13 for the upper one.

To search for $2\nu\beta\beta$ transitions to excited states we have to identify coincidences between two γ-rays in neighboring crystals. As we discussed in Chapter 1, the energies of the photons are $E_{\gamma_1} = 1257.41$ keV and $E_{\gamma_2} = 536.09$ keV (see Figure 2.1). We can imagine different scenarios of coincidence. In the first one, the photon with higher energy, E_{γ_1}, is detected in one crystal and the other photon together with the two emitted electrons are detected in a neighboring crystal (see Figure 5.1). The two electrons emitted in the double beta decay have a probability of nearly zero to exit the crystal where they were produced. Their energy will vary from zero (in practice from the detector threshold) up to the difference between the $Q_{\beta\beta}$ and the energy of the first excited state 0^+ of ^{130}Xe. The maximum value is then $E_{\beta\beta} = 735.3$ keV. This variation occurs because the antineutrinos produced in the decay will have the energy difference.

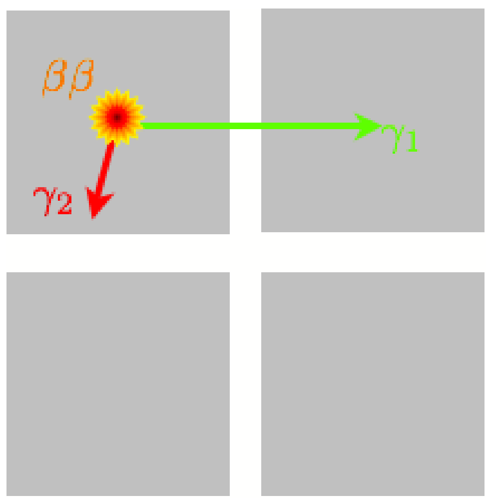

Figure 5.1: A photon with $E_{\gamma_1} = 1257.41$ keV in one crystal in coincidence with a photon with $E_{\gamma_2} = 536.09$ keV in the neighboring crystal along with the energy of the two emitted electrons $E_{\beta\beta} \in [0, 735.3]$ keV.

Another scenario could be γ_1 together with the two electrons in one crystal and γ_2 in a neighboring one (see Figure 5.2).

The most interesting case (but not very probable) is that of the so-called Golden Events: a triple coincidence consisting of the two electrons in one crystal and γ_1 and γ_2 also in different crystals (see Figure 5.3).

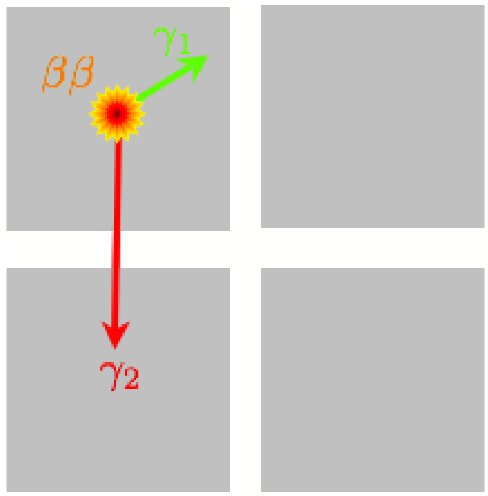

Figure 5.2: A photon with $E_{\gamma_2} = 536.09$ keV in one crystal in coincidence with a photon with $E_{\gamma_1} = 1257.41$ keV in the neighboring crystal along with the energy of the two emitted electrons $E_{\beta\beta} \in [0, 735.3]$ keV.

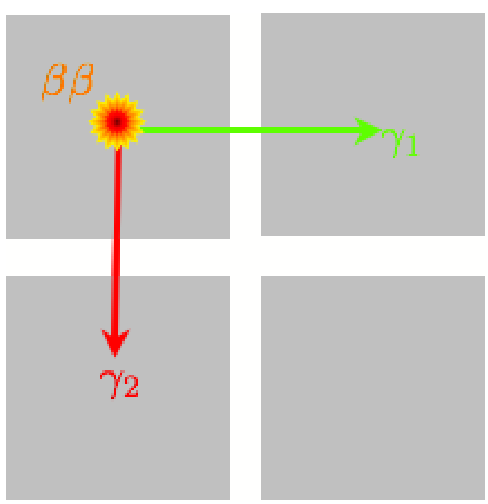

Figure 5.3: ("Golden Events") A photon with $E_{\gamma_2} = 536.09$ keV in one crystal in coincidence with a photon with $E_{\gamma_1} = 1257.41$ keV in the neighboring crystal in coincidence with the energy of the two emitted electrons $E_{\beta\beta} \in [0, 735.3]$ keV in a third neighboring crystal.

The relation to calculate the half life is

$$T^{2\nu}_{1/2} = \frac{\ln 2\, N\, t\, \varepsilon}{c} \tag{5.1}$$

where N is the number of ^{130}Te (emitter) nuclei used as source, t is the time of measurement in years, ε is the efficiency of detecting the process and c is the number of counts under the resulting peak in the spectrum.

To calculate the efficiency, ε, we used a Monte Carlo C++ code based on Geant 4, named Tower-4.7.1. The CUORICINO geometry has been introduced in the code. We have to perform the same type of analysis on the Monte Carlo data as for the real data.

5.3 Preparation Of Data

The analysis was done using ROOT, an object oriented analysis framework.[44] The first goal was to arrange the data in a structure easy to use in the experimental search. The natural structure in ROOT is the TTree. A TTree is used to optimize the data access. A tree uses a hierarchy of branches, and each branch can be read independently from any other branch. So, the first step was to ”translate” the binary files produced in the first level analysis (n-ples) in TTrees. A code was written to achieve this. A separate branch for each parameter describing the pulse was used. This approach has advantages when the parameters are browsed independently, because the access time is shorter. What seemed at the beginning an easy job was in the end more difficult. The binary files (n-ples) were produced on a PC which utilizes a Little Endian byte order (reading numbers from right to left) and were produced the TTrees on a Mac G4, which is using Big Endian byte order (read from left to right). So an algorithm to flip all numbers had to be employed before writing them in the TTree. The good thing about TTrees is that they are machine independent!

It was then decided to add extra parameters that will help in the analysis. It is always important to know if some channels correspond to neighboring crystals or not. This decision is complicated because the data corresponds to Run 1 and Run 2 and, as said before, between runs all wires were exchanged and the order of the acquisition channels changed. For this reason another program was written that contains the maps of the detector in the first and in the second run, respectively. This program searches the channel in the map and adds a new parameter, ”PositionInTower”. All the channels corresponding to the same plane in the tower will have the same value of this parameter. It was then decided to start numbering from the bottom so that that plane has associated value 1. The top plane is then 13. Now, if a crystal has associated the value n of ”PositionInTower”, all crystals having this parameter n, $n-1$ or $n+1$ will be its neighbors.

Finally, it was realized that it would be nice to know immediately which events are single and which are in coincidence having also all of them in the same TTree. For this purpose a parameter called ”Class” was introduced that has the value -1 for single events and positive values for events that are in coincidence. Another code was written that selects the events in disjoint classes using the algorithm presented previously.

The final TTree has the following parameters:

- Class;
- ChannelNumber;
- NumberOfPartials;
- PositionInTower;
- Event;
- Measure number;
- Time;
- AbsoluteTime;
- AmplitudeTimeDomain;

- FrequencyDomainAmplitude;
- SecondPeakAmplitude;
- TestValueLeft;
- TestValueRight;
- Delay;
- DelaySecondPeak;
- Baseline;
- BaselineRMS;
- AmplitudeMm;
- RiseTime;
- DecayTime;
- AmplitudeAF;
- TestValueAF;
- EventType.

The value of the parameter AmplitudeTimeDomain represents, in fact, the energy in keV. For the sorting algorithm, the AbsoluteTime parameter was used which is the sum between Time and Delay. For real events, the parameter EventType is zero. Non-zero values of this last parameter represent pulser events.

For Monte Carlo simulations a program, Tower-4.7.1, written in C++ and based on Geant4, was used, that contains the map of CUORICINO. The output of the Monte Carlo program was transformed into a TTree with the same structure like the real data. The purpose of this approach is to use the same programs used for analysis to calculate the efficiency.

5.4 Maximum Likelihood Method

We present here some details of an analytical maximum likelihood method developed by F. T. Avignone.[10] Consider a set of data points x_i in a spectrum having values $y(x_i)$ (here x_i is a discrete variable corresponding to energy for example). Let us denote the mean background $m(x_i)$. We define $Z_i \equiv y_i - m(x_i)$, where we denoted $y_i = y(x_i)$.

Suppose that we fit the continuum and the peaks in the spectrum. The fitting function is $F(y, \lambda)$, where λ is a parameter. For example, if F is a normalized Gaussian, λ can be the area (number of counts). For some hypothesized value of λ there is an a posteriori probability $P(y_i, F(y_i, \lambda))$ that each point x_i will have the value given by $F(y_i, \lambda)$. In the case of a normal distribution (correct if the number of points is $N > 13$, else we need to use a Poisson distribution),

$$P(y_i, F(y_i, \lambda)) = C_i e^{-\frac{(y_i - F(y_i,\lambda))^2}{2\sigma_i^2}}, \tag{5.2}$$

where C_i is a constant.

The likelihood function $\mathcal{L}(\lambda)$ is defined as:

$$\begin{aligned} \mathcal{L} &= \prod_i P(y_i, F(y_i, \lambda)) = C \prod_i e^{-\frac{(y_i - F(y_i, lambda))^2}{2\sigma_i^2}} \\ &= C e^{-\sum_i \left(\frac{(y_i - F(y_i,\lambda))^2}{2\sigma_i^2} \right)}. \end{aligned} \tag{5.3}$$

At the exponent we have the chi square

$$\chi^2 \equiv \sum_i \frac{(y_i - F(y_i, \lambda))^2}{2\sigma_i^2}. \tag{5.4}$$

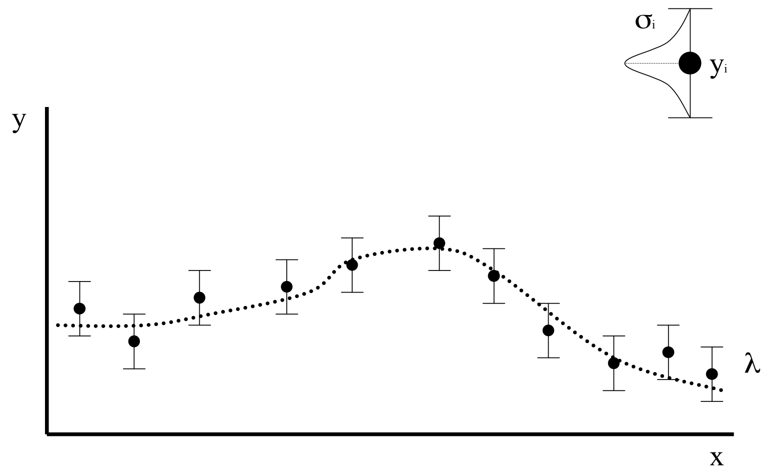

Figure 5.4: Fitting function depending on parameter λ.

We consider the logarithm of the likelihood function

$$\ln \mathcal{L} = C' - \sum_i \frac{(y_i - F(y_i, \lambda))^2}{2\sigma_i^2},$$
$$= C' - \chi^2. \tag{5.5}$$

The function $\ln \mathcal{L}$ will be maximum when χ^2 will be minimum. The likelihood $\mathcal{L}$ will have the same maximum (maximum likelihood) as $\ln \mathcal{L}$, obtained for λ_0.

In[10] we consider a peak of Gaussian shape and a mean background m. The quantities a

and b are defined as

$$a \equiv \frac{1}{\sigma_y^2\sqrt{2\pi}}\sum_{i=1}^{n} Z_i e^{-\frac{(x_i-x_0)^2}{2\sigma_x^2}},$$

$$b \equiv \frac{1}{2\pi\sigma_y^2\sigma_x}\sum_{i=1}^{n} e^{-\frac{(x_i-x_0)^2}{\sigma_x^2}}, \tag{5.6}$$

where σ_y is averaged σ_i, and x_0 is the center of the studied peak. With these quantities the logarithm of the likelihood function (5.5) is expressed as:[10]

$$\ln \mathcal{L} = a\lambda - \frac{1}{2}\lambda^2. \tag{5.7}$$

The likelihood function is then

$$\mathcal{L} = e^{a^2/2b} e^{-\frac{1}{2}b(\lambda-\lambda_0)^2}, \tag{5.8}$$

where λ_0 is the value of the parameter that maximizes $\mathcal{L}$.

If we denote

$$\eta_i \equiv e^{-\frac{(x_i-x_0)^2}{2\sigma_x^2}}, \tag{5.9}$$

we have

$$a = \frac{1}{\sigma_y^2\sqrt{2\pi}}\sum_i Z_i\eta_i,$$

$$b = \frac{1}{2\pi\sigma_y^2\sigma_x}\sum_i \eta_i^2. \tag{5.10}$$

It is shown that the value λ_0 that will give the maximum likelihood is calculated as

$$\lambda_0 = \frac{a}{b}. \tag{5.11}$$

Having determined λ_0, the most likely value of λ, we then wish to calculate the confidence interval $\lambda(\text{C.L.})$. There are several ways of doing it. One of them is to calculate the ratio of the integrals

$$\text{C.L.} = \frac{\int_{\lambda_0}^{\lambda(\text{C.L.})} L(\lambda) d\lambda}{\int_{\lambda_0}^{\infty} L(\lambda) d\lambda}. \tag{5.12}$$

It is convenient to initiate a change of variables in which $u \equiv b^{1/2}((\lambda - \lambda_0))$ and $u(\text{C.L.}) = b^{1/2}(\lambda(\text{C.L.}) - \lambda_0)$. Using this substitution, we see

$$\text{C.L.} = \sqrt{\frac{2}{\pi}} \int_0^{u(\text{C.L.})} e^{-\frac{1}{2}u^2} du = \sqrt{\frac{1}{2\pi}} \int_{-u(\text{C.L.})}^{u(\text{C.L.})} e^{-\frac{1}{2}u^2} du. \tag{5.13}$$

To determine $u(\text{C.L.})$ and hence $\lambda(\text{C.L.})$, one selects the desired confidence interval $C.L.$ and obtains $u(\text{C.L.})$ directly from normal distribution tables. Then calculate

$$\lambda(\text{C.L.}) = \frac{u(\text{C.L.})}{\sqrt{b}} + \lambda_0. \tag{5.14}$$

From the tables we have

$$u(0.68) = 1,$$

$$u(0.90) = 1.645, \tag{5.15}$$

$$u(0.95) = 1.96.$$

Chapter 6

Results

CUORICINO was cooled down at the beginning of 2003. During the cooling process some of signal wires disconnected so that in this first run only 32 large crystals and 16 small ones could be read. The total active mass was 8.73 kg of ^{130}Te. The performance in the first run was good. The average FWHM resolution measured during the calibration of the detectors with a ^{232}Th source was ~ 7 keV for large crystals and ~ 9 for small ones. Both these values were measured with the ^{208}Tl background gamma line at 2615 keV. An evaluation of the average FWHM resolution at low energy in a calibration measurement is not possible because the radioactive source used for calibration is located far away from the detectors and low energy gammas are absorbed before reaching them. The sum calibration spectra of all large and small available crystals, respectively are shown in Figure 6.1.

The detector response and FWHM, evaluated in calibration are shown in Tab. 6.1, 6.2, 6.3 and 6.4 at the end of this chapter.

On April 19th 2003 the first background measurement started (Run I). The live time was $\sim 72\%$, including the time required for periodic calibration (every 15 days) of the detectors. The data collected from three of the functioning detectors was not used because two detectors were cross-talking and the third presented excessive spurious noise. Thus, only 29 of the large crystals were used for the study of the background. Referring to the small crystals, one of them presented a variation in the reference pulse position. Also, after

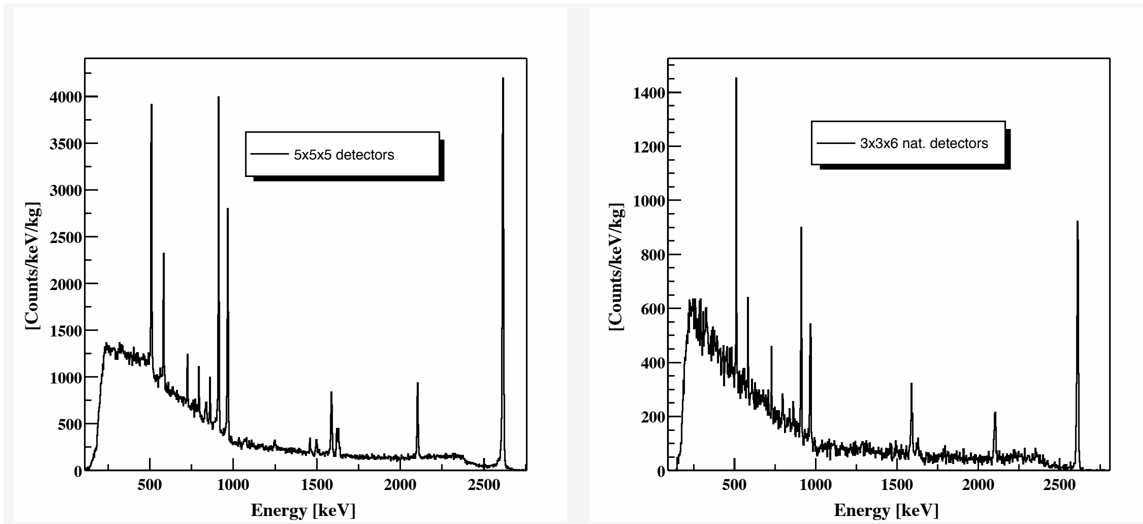

Figure 6.1: Summed calibration spectra (^{232}Th source) from all operating $5\times5\times5$ cm^{3}and $3 \times 3 \times 6$ cm^3 crystals, respectively.

some weeks of measurements, one of the two central detectors lost its heater. Therefore, in this run we had 11 small natural crystals and 4 enriched ones working.

At the end of October 2003 CUORICINO was stopped to undergo substantial maintenance operations, and to recover the lost electrical connections. In November 2003 the array was warmed up to room temperature to repair the connections and also some cryogenic problems were fixed. These operations required several months.

At the end of April 2004 CUORICINO started taking data again (Run II). This time, in the process of cooling two of the $5 \times 5 \times 5$ cm^3 crystal and one $3 \times 3 \times 6$ cm^3 wires were disconnected. In fact there were 40 large and 17 small crystals working, the total active mass corresponding to 11.3 kg of ^{130}Te.

The collected statistics in this second run is 1.35 kg $\cdot$ y for $5 \times 5 \times 5$ cm^3 and 0.19 kg $\cdot$ y for $3 \times 3 \times 6$ cm^3 crystals, respectively. The average FWHM resolution measured during calibration with a ^{232}Th source was ~ 8 keV for large crystals and ~ 11 keV for the small ones.

The total exposure from the beginning of Run I up to October 2005 was 5.97 kg yr

(^{130}Te), equivalent to

$$N(^{130}Te)t = 2.764 \times 10^{25} \text{ yr.} \tag{6.1}$$

6.1 $2\nu\beta\beta$-Decay To Excited 0^+ State Of ^{130}Xe

Initially, three scenarios were considered, but because the probability of γ-ray $E_{\gamma_2} = 536.09$ keV γ-ray escaping from the crystal it was produced in is very small, only the first scenario could be used. No "golden events" were found for the same reason. Thus, we looked for a coincidence between a γ-ray with the energy $E_{\gamma_1} = 1257.41$ keV in one crystal with the other γ-ray, $E_{\gamma_2} = 536.09$ keV, plus the energy of the two electrons, $E_{\beta\beta} \in [\text{threshold}, 735.3]$ keV, in a neighboring crystal. As already discussed in the previous chapter, the difference between the upper value, 735.3 keV, and $E_{\beta\beta}$ is found in the energy of the antineutrinos.

A code was used that acted as a filter, selecting only events with the energy in the range $[1230, 1280]$ keV which are in coincidence with events with the energy between the energy of γ_2, and the sum of the maximum energy of the electrons and the energy of γ_2, $E \in [536.09, 1271.39]$. The coincidence spectrum was constructed and a peak was searched for at $E_{\gamma_1} = 1257.41$ keV.

The biggest peak in this spectrum at 1238 keV corresponds to ^{234}Bi from the ^{238}U chain (see Figure 6.2). The background is almost linear. To fit the background, we considered a linear polynomial and a Gaussian centered on 1238 keV. If there is a peak at 1257.41 then we can fit it with another Gaussian (see Figure 6.3).

To find the efficiency of the decay, a Monte Carlo simulation was performed using the code Tower-4.7.1. With the data obtained from the simulation, the same type of analysis was done as with real data. The coincidence spectrum for the Monte Carlo in this scenario

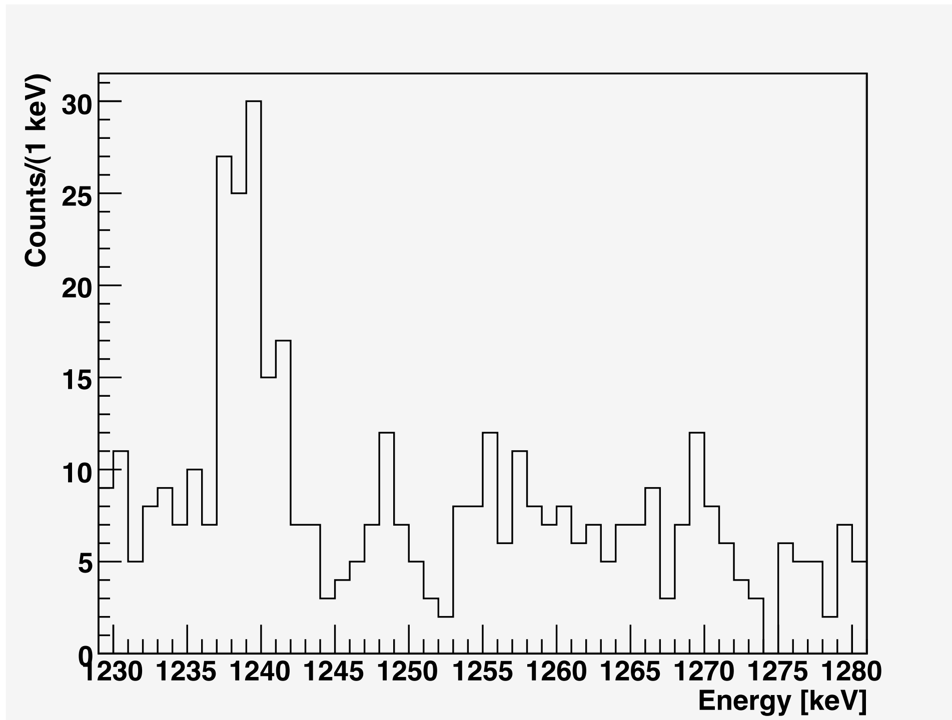

Figure 6.2: Coincidence spectrum.

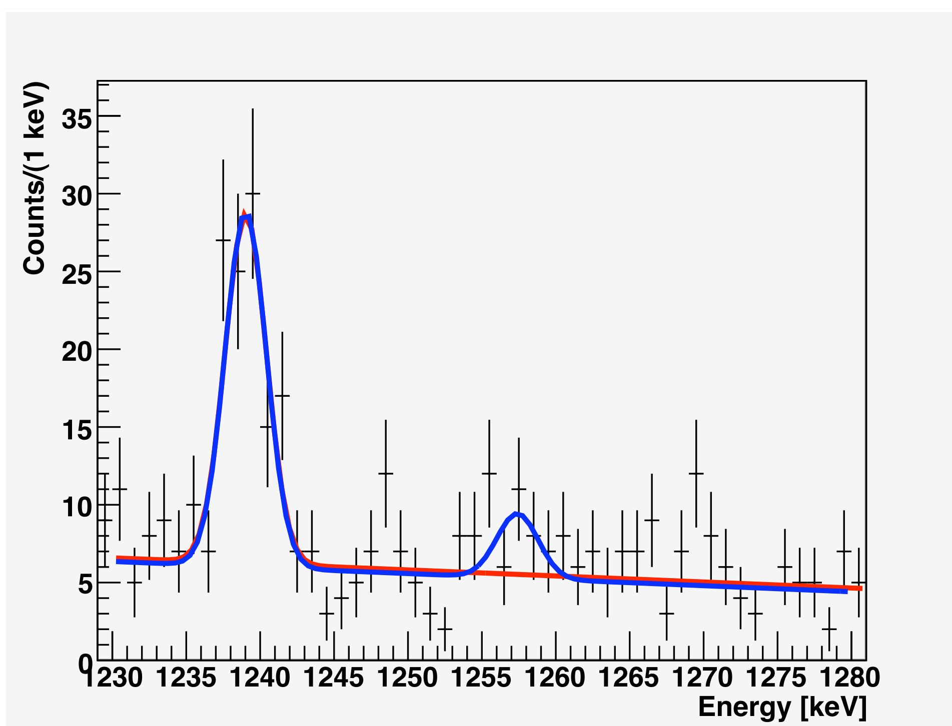

Figure 6.3: Coincidence spectrum, best fit.

is shown in Figure 6.4. The obtained efficiency is

$$\varepsilon = 0.011. \tag{6.2}$$

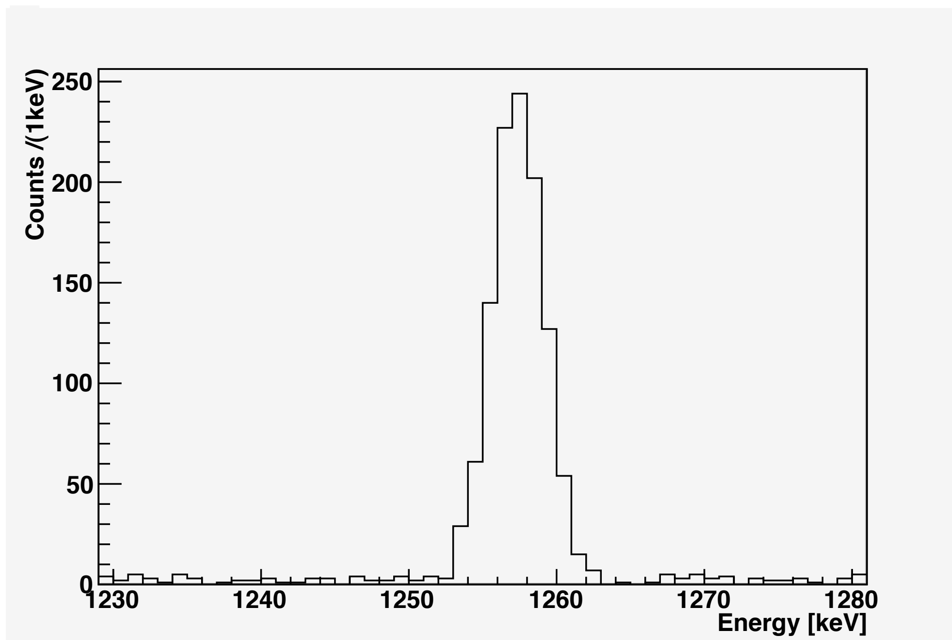

Figure 6.4: Monte Carlo analysis.

From the best fit we obtained the following number of counts under the peak at 1257.41 keV

$$c = 14.51 \pm 6.68 \text{ counts.} \tag{6.3}$$

Using (5.1)

$$T_{1/2}^{2\nu} = \frac{\ln 2 NT\varepsilon}{c}, \tag{6.4}$$

with the number of counts, c is given in (6.3), Nt in (6.1) and ε in (6.2), respectively, we obtain:

$$T_{1/2}^{2\nu} = \left(1.45^{+1.24}_{-0.46}\right) \times 10^{22} \text{ yr.} \tag{6.5}$$

The lower limit on the half life of $2\nu\beta\beta$-decay of ^{130}Te to the excited 0^+ state of ^{130}Xe is:

$$T^{2\nu}_{1/2} \geq 0.90 \times 10^{22} \text{ yr } (90\% \text{ C.L.}).$$

6.2 $0\nu\beta\beta$-decay

No peak appears in the anticoincidence background spectrum in correspondence with ^{130}Te $0\nu\beta\beta$ searched line at 2528.8 keV.

The sum of the spectra of the $5 \times 5 \times 5$ cm^3 and $3 \times 3 \times 6$ cm^3 crystals in the region of the the $0\nu\beta\beta$-decay energy is shown in the Figure 6.5. One can clearly see the peaks at 2447 and 2615 keV from the decays of ^{214}Bi and ^{208}Tl, plus a small peak at 2505 keV due to the sum of the two γ lines of ^{60}Co. The efficiency of the detector for this decay is $\varepsilon = 0.85$. To calculate the half life we used a relation similar to (5.1),

$$T^{0\nu}_{1/2} = \frac{\ln 2 N t \varepsilon}{c}, \tag{6.6}$$

where c is the number of candidate events in a peak centered at 2529 keV, and the value of Nt is given in (6.1). We use a maximum likelihood analysis, fitting the peaks and continuum in the spectrum in the region of the spectrum from 2430 to 2460 keV (see Figure 6.5) and we obtain a negative peak with

$$c = -13.35 \pm 5.45$$

counts.

6.2.1 Analysis # 1

Because the peak is so negative, we artificially consider the background to be equal to the mean background and thus to 90% C.L. we will use the sigma obtained from the likelihood

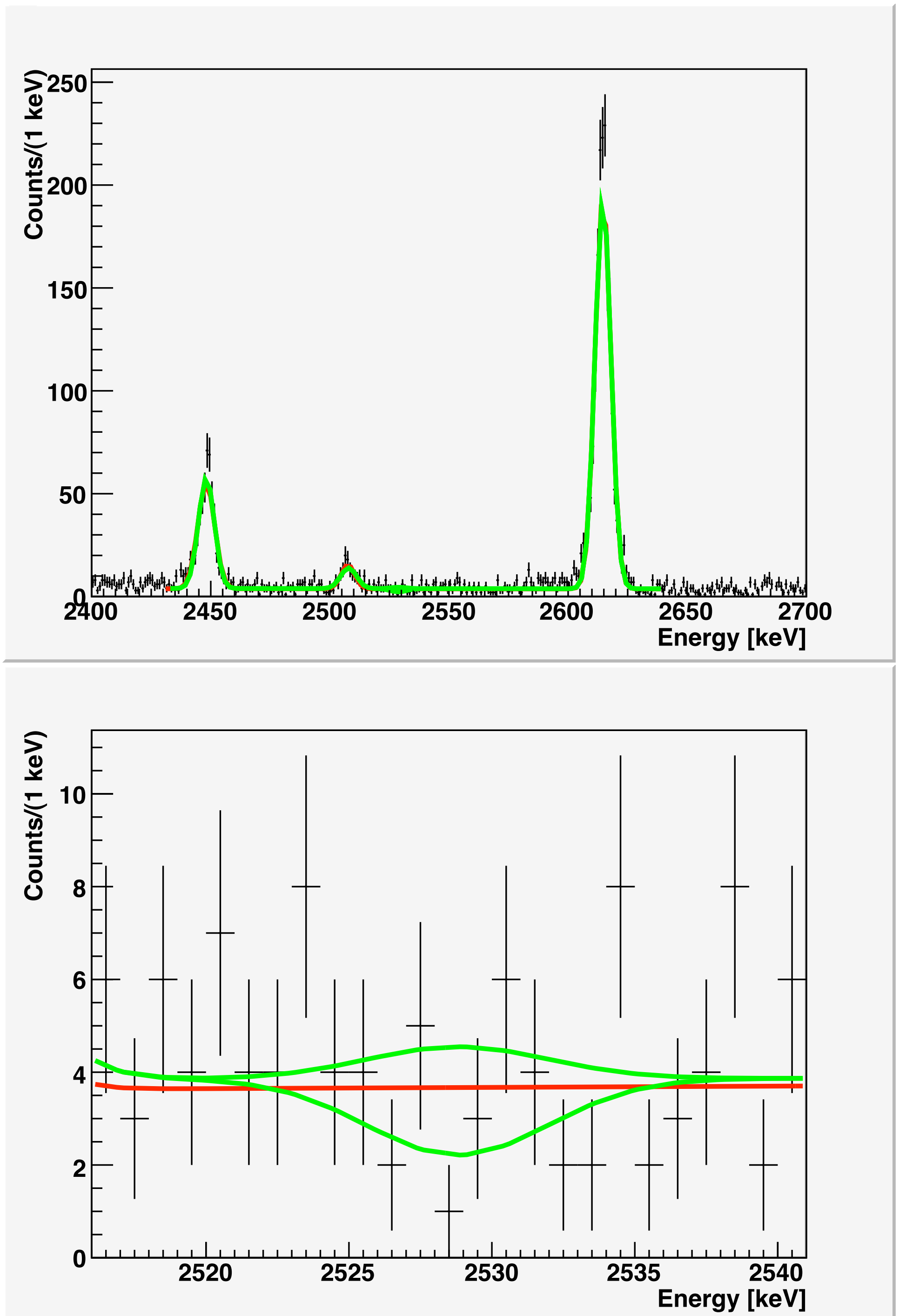

Figure 6.5: Summed background spectrum for all operating crystals in the region of neutrinoless double beta decay of ^{130}Te (Q-value$= 2528.8$ keV).

function, 5.45, multiplied by 1.645:

$$c = 0 + 5.45 \times 1.645 = 8.97 \text{ counts.}$$

Inserting this value in (6.6) we obtain

$$T_{1/2}^{0\nu} \geq 1.82 \times 10^{24} \text{ yr } (90\% \text{ C.L.})$$

This is the most conservative result.

6.2.2 Analysis # 2

Let us consider that we have a null experiment. Then

$$\frac{-13.35}{5.45} = -2.45\sigma.$$

This means that we have 0 counts to 98.5 C.L. The number of counts is given as a function of C.L. by

$$c \simeq \ln \{1/(1 - \text{C.L.})\}.$$

For 3σ we obtain $c = 5.9$ counts. Inserting this value in (6.6) we obtain

$$T_{1/2}^{0\nu} > 2.76 \times 10^{24} \text{ yr } (3\sigma),$$

if considered it to be a null experiment. However, it is not actually a null experiment so we also do the following analysis.

6.2.3 Analysis # 3

We use here the maximum likelihood technique[10] described in the previous chapter. We have

$$c \leq 0.80 \text{ counts } (68\% \text{ C.L.})$$

$$c \leq 4.23 \text{ counts } (90\% \text{ C.L.})$$

$$c \leq 5.33 \text{ counts } (95\% \text{ C.L.})$$

So, for 95% C.L. we have

$$T^{0\nu}_{1/2} \geq 3.1 \times 10^{24} \text{ yr } (95\% \text{ C.L.})$$

Run I					
Channel	**F**WHM [keV]	**T**ime op. [h]	**P**lane	**C**rystal	**T**ype
9		N	1	B25	large
21	5.1	1322.04	1	B29	large
20	6.8	1322.04	1	B42	large
51		N	1	B32	large
8	18.8	863.37	2	130-2	small enrich.
33	9.8	863.37	2	B	small
22	12.8	863.37	2	128-2	small enrich.
34	13.5	863.37	2	16	small
50		863.37	2	14	small
49	6.2	863.37	2	13	small
52	8.7	863.37	2	128-1	small enrich.
10	7.8	863.37	2	F	small
19	13.5	764.59	2	130-1	small enrich.
48	7.1	863.37	3	E	small
23	7.9	634.11	3	4	small
35	13.1	863.37	3	O	small
36	4.6	N	3	I	small
7	9.5	863.37	3	5	small
6		N	3	H	small
31	7.7	863.37	3	6	small
11	8.3	863.37	3	2	small
53	8.1	634.11	3	9	small
12	17.2	1322.04	4	B47	large
47	5.6	1322.04	4	B54	large
37	8.8	1322.04	4	B36	large
18	7.2	N	4	B28	large
5		N	5	B24	large
24	7.7	1322.04	5	B27	large
30		N	5	B43	large
54	5.6	1322.04	5	B31	large
46		N	6	B30	large
61	5.4	1322.04	6	B26	large
17	7.1	1322.04	6	B46	large
67	5.3	1322.04	6	B45	large

Table 6.1: Detectors performance and time of operation in Run 1 (part 1).

Run I					
Channel	**F**WHM [keV]	**T**ime op. [h]	**P**lane	**C**rystal	**T**ype
4		N	7	B14	large
62	5.8	1322.04	7	B10	large
16	6.4	1322.04	7	B56	large
55	7.5	1322.04	7	B12	large
45	6.2	1322.04	8	B16	large
66	11.9	N	8	B17	large
15		N	8	B62	large
68	7.1	1322.04	8	B61	large
3		N	9	B38	large
63	5.8	1322.04	9	B40	large
27	9.8	1223.27	9	B51	large
56	7.2	1322.04	9	B52	large
44	10.2	1322.04	10	B55	large
64	11.9	N	10	B37	large
14	7.5	1322.04	10	B60	large
69	5	1322.04	10	B53	large
2	14	898.14	11	B15	large
41	7	1322.04	11	B18	large
26	6	1322.04	11	B44	large
57	8.7	1322.04	11	B41	large
43		N	12	B35	large
65		N	12	B49	large
13	7.3	1322.04	12	B7	large
70	5.7	1322.04	12	B34	large
1		N	13	B23	large
58	7	1322.04	13	B57	large
25		N	13	B39	large
42	7	1322.04	13	B13	large

Table 6.2: Detectors performance and time of operation in Run 1 (part 2).

Run II					
Channel	**F**WHM [keV]	**T**ime op. [h]	**P**lane	**C**rystal	**T**ype
21	17.1	4455.75	1	B25	large
34	9.42	3992.47	1	B29	large
10	7.79	4455.75	1	B42	large
51	8.23	4426.64	1	B32	large
20	16.12	4455.75	2	130-2	small enrich.
11	8.67	4453.35	2	B	small
35	16.7	4426.64	2	128-2	small enrich.
12	20	3970.53	2	16	small
50		4057.99	2	14	small
49	6.87	4426.64	2	13	small
33	13.56	4426.64	2	128-1	small enrich.
22	6.93	2109.08	2	F	small
52	14.1	4426.64	2	130-1	small enrich.
48	6.77	4426.64	3	E	small
36	8.46	4426.64	3	4	small
61	12.23	3871.37	3	O	small
37	5.25	3855.44	3	I	small
19	13.02	3027.47	3	5	small
18	9.21	4455.75	3	H	small
9	10	3028.47	3	6	small
23	7.33	3028.47	3	2	small
53	8.15	3855.44	3	9	small
47		4021.58	4	B47	large
62	5.59	4426.64	4	B54	large
32	11.6	3970.53	4	B36	large
24	6.06	4426.64	4	B28	large
17	5.34	3424.06	5	B24	large
38	6.16	3992.47	5	B27	large
8	8.86	4455.75	5	B43	large
15	5.96	4455.75	5	B31	large
46	7.61	4426.64	6	B30	large
63	5.97	4021.58	6	B26	large
31	7.07	4426.64	6	B46	large
67	5.7	4477.58	6	B45	large

Table 6.3: Detectors performance and time of operation in Run 2 (part 1).

Run II					
Channel	**F**WHM [keV]	**T**ime op. [h]	**P**lane	**C**rystal	**T**ype
16	5.73	4448.93	7	B14	large
39		N	7	B10	large
7	5.08	4014.76	7	B56	large
55	5.67	4419.82	7	B12	large
45	7.37	3851.86	8	B16	large
64	11.5	3825.27	8	B17	large
6	4.93	3851.86	8	B62	large
68	7.79	3955.75	8	B61	large
54		N	9	B38	large
40	7.28	4318.02	9	B40	large
5	5.77	4389.92	9	B51	large
56	5.83	4360.81	9	B52	large
44	7.47	4360.81	10	B55	large
65	13.12	4411.75	10	B37	large
4	8.8	4389.92	10	B60	large
57	7.17	3926.64	10	B53	large
14	10.4	3516.48	11	B15	large
41	8.97	3926.64	11	B18	large
3		N	11	B44	large
58	16.17	4360.81	11	B41	large
43	13.21	3338.57	12	B35	large
66	19.69	4347.1	12	B49	large
2		N	12	B7	large
59	10.39	3982.91	12	B34	large
13	7.95	3995.26	13	B23	large
60		4036.16	13	B57	large
1		2970.79	13	B39	large
42	7.77	4219.93	13	B13	large

Table 6.4: Detectors performance and time of operation in Run 2 (part 2).

Chapter 7

Conclusion

7.1 Summary of the Thesis

The main goal of this dissertation was the analysis of the $2\nu\beta\beta$-decay of ^{130}Te to the first 0^+ excited state at 1793.50 keV of ^{130}Xe using the data from CUORICINO experiment.

In the first chapter the general properties of neutrinos are presented along with a short history. A brief history of the subject of double-beta $(\beta\beta)$ decay is given, followed by discussion of different modes of decay and a table with double-beta decay candidates.

In the second chapter the salient points of the underlying theoretical formalism and its connection to the theory of neutrinos, and in particular its direct connection of neutrino mixing matrix. A brief discussion is given of the foundations of the Quasi Particle Random Phase Approximation (QRPA) method of calculating the relevant nuclear transition matrix elements.

In the third chapter a detailed description of the Bolometric Technique of detecting particles and radiation is given, and its direct application to $\beta\beta$-decay.

The structure and construction of the CUORICINO bolometric detector is discussed in detail in the fourth chapter. The detector comprises 13 planes of TeO_2 bolometers containing 40.7 kg of crystals, with a total of 11 kg of ^{130}Te.

In the next chapter the off-line analysis is presented. It consists of two levels, the author being involved mainly in the second level. Some of the algorithms of organizing data are also presented. The research scenarios for the analysis of the $2\nu\beta\beta$-decay of ^{130}Te to the first 0^{+} excited state of ^{130}Xe, were also discussed.

In Chapter 6 the results of the analysis are presented. Because of the very small values of the efficiencies, only one scenario was used in the search. The efficiency was found to be $\varepsilon = 0.011$. The final result for the$2\nu\beta\beta$-decay to the excited state is: $T^{2\nu}_{1/2} = \left(1.45^{+1.23}_{-0.46}\right) \times 10^{22}$ y. While this a positive result, it is not statistically significant. In any case a lower limit can be stated: $T^{2\nu}_{1/2} \geq 0.90 \times 10^{22}$ y (90% C.L.). If the small positive peak in the data is due to $\beta\beta$-decay, two more years of running should give a conclusive observation. Finally, data were analyzed to search for $0\nu\beta\beta$-decay of ^{130}Te to the ^{130}Xe ground state. Three interpretations of the data were used with the resulting lower bound of $T^{0\nu}_{1/2}(^{130}Te) \geq 1.84 \times 10^{24}$ y using the most conservative one. If the peak in the data is due to $2\nu\beta\beta$-decay to the 0^{+} state at 1793.5 keV, two more years of running should give a conclusive observation. The data were analyzed to search for $0\nu\beta\beta$-decay of ^{130}Te to the ^{130}Xe ground state with the resulting lower bound of $T^{0\nu}_{1/2}(^{130}Te) \geq 1.84 \times 10^{24}$ y using the most conservative interpretation of the data.

7.2 Contributions

The main contributions of this dissertation can be summarized as follows:

- We obtained the half life of the $2\nu\beta\beta$-decay of ^{130}Te to the first 0^{+} excited state at 1793.50 keV of ^{130}Xe.

- We obtained the lower limit of the decay of ^{130}Te to the ^{130}Xe ground state.

- We organized the data for this analysis using ROOT TTrees and we created programs for sorting and coincidences.

Bibliography

1. S. N. Ahmed *et al.*, arXiv:nucl-ex/0309004; *Phys. Rev. Lett.* **89** (2002), 011301.
2. M. H. Ahn *et al.*, *Phys.Rev.Lett.* **90** (2003), 041801.
3. A. Alessandrello *et al.*, *Nucl. Instr. and Meth.* **A** 414 (1998) 454-464.
4. M. Ambrosio *et al.*, *Phys. Lett. B* **566** (2003), 35.
5. M. Apollonio *et al.*, *Phys. Lett. B* **466** (1999), 415.
6. C. Arnaboldi *et al.*, *Phys.Lett. B* **584** (2004) 260-268.
7. C. Arnaboldi *et al.*, *Phys. Lett. B* **557** (2003) 167-175.
8. D. R. Artusa, *MS Thesis*, University of South Carolina, Columbia 2004.
9. F. T. Avignone, R. L. Brodzinski, *Progr. Part. Nucl. Phys* **21** (1988), 99-181.
10. F. T. Avignone, *Nucl. Instr. and Meth.* **A** (1986), 525-529.
11. S. Baker and P.D. Cousins, *Nucl. Instrum. and Meth.* **221** (1984) 437.
12. A. S. Barabash, arXiv: hep-ex/0602037, (2006).
13. A. S. Barabash *et al.*, *Eur. Phys. J. A* **11**, (2001), 143-145.
14. A. S. Barabsh *et al.*, *Phys. Lett. B* **345**, (1995), 408.
15. V. Barger, S. L. Glashow, D. Marfatia, and K. Whisnant, *Phys. Lett. B* **532** (2002), 15.
16. R.M. Barnett *et al.*, (PDG), *Phys. Rev. D* **54** (1996) 1.
17. Bernatowicz *et al.*, *Phys. Rev. C* **47** (2003), 1993.
18. David O. Cadwell (Ed.), *Current Aspects of Neutrino Physics*, Springer-Verlag Berlin Heidelberg New York, 2001, ISBN 3540410023.
19. J. M. Cork *et al.*, *Phys. Rev.* **107** (1957), 1621.
20. M. Doi, T. Kotani and E. Takasugi, *Progr. Theor. Phys.* **83** (1985), 1.
21. S. Capelli, *PhD Dissertation*, Università di Milano Biccoca, Milan 2005.
22. Ling-Lie Chau and Wai-Yee Keung, *Phys. Rev. Lett.* **53** (1984), 1802.

23. O. Cremonesi, *Nucl. Phys. B* **118** (2003), 287-296.

24. K. Eguchi *et al.*, *Phys.Rev.Lett.* **90** (2003), 021802, and arXiv:hep-ex/0310047.

25. H. Ejiri, *Prog. in Part. and Nucl. Phys. B* **48** (2002), 185.

26. S. R. Elliot and P. Vogel, *Ann. Rev. Nucl. Part. Sci.* **52** (2002), hep-ph/0202264.

27. J. Engel, P. Vogel, M. R. Zirnbauer, *Phys. Rev. C* **37** (1998), 731.

28. A. Faessler and F. Šimkovic, *J. Phys. G* **24** (1998), 24-2139.

29. G.J. Feldman and R.D. Cousins, *Phys. Rev. D* **57** (1998) 3873.

30. E. Fiorini and T. Niinikoski, *Nucl. Instrum. and Methods Phys. Res. A* **224** (1984), 83.

31. M. Fukugita, A. Suzuki (Eds) *Physics and Astrophysics of Neutrinos*, Springer-Verlag, 1994, ISBN 4431701362.

32. E.Gatti and P.F.Manfredi, *Rivista Nuovo Cimento* **9** (1986), 1.

33. M. Goepert-Mayer, *Phys. Rev* **48** (1935), 512.

34. P. Gorla, *PhD Dissertation*, Università di Milano Biccoca, Milan 2005.

35. D.E. Groom *et al.*, *Eur. Phys. J C* **15** (2000) 1.

36. Y. Hayato *et al.*, Talk given at the Int. EPS Conference on High Energy Physics, July 17 - 23, 2003, Aachen, Germany.

37. Klapdor-Kleingrothaus *et al.*, *Nucl.Instrum.and Meth.* **522** (2004) 367.

38. M. Maltoni, T. Schwetz, M. A. Tortola and J. W. F. Valle, arXiv:hep-ph/0309130 (2003); *Nucl. Phys. Proc. Suppl.* **114** (2003), 203.

39. M. Moe and P. Vogel, *Ann. Rev. Nucl. Part. Sci.* (1994), 44-247.

40. S. Pascoli and S. T. Petcov, *Phys. Lett. B* **544** (2002), 239, and Addendum, arXiv:hep-ph/0310003.

41. M. Pedretti, *PhD Dissertation*, Università di Milano Biccoca, Milan 2004, and references therein.

42. W.H. Press, B.P. Flannery, S.A. Teukosky and W.T. Vetterling, *Numerical Recipes in C , The Art of Scientific Computing* - Cambridge University Press 1991.

43. H. Primakoff and S. P. Rosen, *Rep. Progr. Phys.* **22** (1959), 121.

44. ROOT Users Guide 5.08, 2006.

45. M. B. Smy *et al.*, arXiv:hep-ex/0309011.

46. J. Suhonen, M. Aunola, *Nucl. Phys. A* **723** (2003), 271-288.

47. J. Suhonen, *Phys. Rev. C* **62**, (2000) 042501.

48. J. Suhonen, O. Civitarese, *Phys. Rep.* **300** (1998), 123-214.

49. T. Tomoda, *Rep. Prog. Phys.* **54**, (1991), 53-126.

50. V. I. Tretyak and Yu. G. Zdesenko, *Atomic Data and Nuclear Data Tables*, **80** (2002) 83.

51. Yu. G. Zdesenko, *Rev. Mod. Phys.*, **74** (2002) 663.